Lithos 227 (2015) 255–268

Contents lists available at ScienceDirect

Lithos

journal homepage: www.elsevier.com/locate/lithos

Protracted late magmatic stage of the Caleu pluton (central Chile) as a consequence of heat redistribution by diking: Insights from zircon data and thermal modeling

Pablo G. Molina [a], Miguel A. Parada [a], Francisco J. Gutiérrez [a,b,*], Changqian Ma [c], Jianwei Li [c], Liu Yuanyuan [c], Martin Reich [a], Álvaro Aravena [a]

[a] Departamento de Geología, Centro de Excelencia en Geotermia de los Andes (CEGA), Universidad de Chile, Plaza Ercilla 803, Santiago, Chile
[b] Advanced Mining Technology Center (AMTC), Facultad de Ciencias Físicas y Matemáticas, Universidad de Chile, Santiago 8370451, Chile
[c] State Key Laboratory of Geological Processes and Mineral Resources, China University of Geosciences, Wuhan, People's Republic of China

ARTICLE INFO

Article history:
Received 30 June 2014
Accepted 12 April 2015
Available online 25 April 2015

Keywords:
Caleu pluton
Zircon U–Pb dating
Diking
Thermal modeling
Crystal mush

ABSTRACT

Zircon U–Pb geochronology and geochemistry are combined with whole-rock composition and thermal modeling to decipher the late magmatic stage of the composite Cretaceous Caleu pluton, which consists of four lithological zones: Gabbro–Diorite Zone (GDZ), Quartz Monzodiorite Zone (QMDZ), Granodiorite Zone (GZ) and Monzogranite Zone (MGZ). The four lithological zones include felsic dikes and veins of variable thickness and distribution. Zircons of four representative samples, each from the mentioned zones, were dated and chemically analyzed. The U–Pb ages exhibit sample-scale scatter derived from protracted zircon crystallization. At pluton scale the ages are substantially overlapped with a subtle decrease of ages from mafic to felsic sample; the latter has a normal age span distribution with a mean age of 94.68 ± 0.71 (2σ confidence) and a MSWD of 0.95. Zircon grains from the uppermost zone of the pluton, where the QMDZ is emplaced, have the highest REE and HFSE contents. Zircon crystallization temperatures oscillate between 680 and 850 °C, regardless of the zircon age and sample composition. Differences in temperature and age of zircon crystallization of up to 185 °C and 2.6 Myr were identified at sample scale, respectively. Numerical modeling indicates that the melts from which zircon crystallized are highly crystalline (mostly higher than 60% crystal) and resemble MGZ in compositions. Time-dependent thermal models were performed to account for preservation of the system above solidus temperature for long time intervals consistent with those of zircon crystallization. Two non-exclusive scenarios for the late-stage development of Caleu pluton were considered: (i) pluton construction by magma pulses assembled incrementally and (ii) upward transport of residual melts by diking through a mush system to yield heat redistribution to the levels where the samples collected. The first scenario does not preserve residual melts for intervals as long as 2.6 Myr unless an extremely thick magma reservoir is considered. The second scenario is more favorable because it could provide enough heat that allows preserving residual melts above the solidus temperature depending on: (i) dike width, (ii) melt transport velocity and (iii) dike intensity (vol.% dike). For a dike width of 0.2 m and dike intensity of 10%, consistent with field observations, a transport velocity of 300 m/yr is required to maintain the upper mush zone above 700 °C. The melt transport would have occurred as successive events to allow developing the protracted late magmatic stage of the Caleu pluton.

1. Introduction

In the last decade, the time-scale for pluton construction has been unraveled by U–Pb zircon ages that show highly variable time intervals from tens of thousands of years for small intrusions (e.g., Michel et al., 2008), to more than 10^6 years for large bodies (e.g., Coleman et al., 2004; Díaz Alvarado et al., 2013; Glazner et al., 2004; Miller et al., 2007). The large intervals of pluton construction could have resulted from the amalgamation of magma increments with distinct ages (Annen, 2011; Barboni et al., 2013; Bergantz, 2000; Díaz Alvarado et al., 2013; Glazner et al., 2004; Matzel et al., 2006; Michel et al., 2008; Miller et al., 2011; Parada et al., 2005b; Paterson and Vernon, 1995; Walker et al., 2007), producing longer magma residence in the crust than those calculated from thermal modeling of a single body emplaced instantaneously (e.g., Glazner et al., 2004). The systematic

* Corresponding author at: Advanced Mining Technology Center (AMTC), Facultad de Ciencias Físicas y Matemáticas, Universidad de Chile, Santiago 8370451, Chile.
E-mail addresses: pamolina@ing.uchile.cl (P.G. Molina), maparada@ing.uchile.cl (M.A. Parada), frgutier@ing.uchile.cl (F.J. Gutiérrez), cqma1978@gmail.com (C. Ma), jwli@cug.edu.cn (J. Li), geoliuyy@gmail.com (L. Yuanyuan), mreich@ing.uchile.cl (M. Reich), a.aravena.ponce@gmail.com (Á. Aravena).

http://dx.doi.org/10.1016/j.lithos.2015.04.008
0024-4937/

zircon U–Pb ages recorded in many plutons have contributed to the understanding that their anatomy resulted from incrementally emplaced magma batches that allowed melt preservation at time of a new injection (Annen et al., 2006; Gelman et al., 2013b; Wiebe and Collins, 1998) or as a consequence of incremental growth once the preceding pulse was solidified (Glazner et al., 2004; Michel et al., 2008). Additionally, many multiple-pulse magma systems could give rise to a large volume of volcanic products due to rejuvenation of crystal-rich melts by replenishment of fresh and hot magma (Burgisser and Bergantz, 2011; Claiborne et al., 2010a, 2010b; Díaz Alvarado et al., 2013; Gelman et al., 2013a; Huber et al., 2010, 2011; Miller et al., 2011; Peytcheva et al., 2008).

A more complete late history of a magmatic system could be addressed through zircon studies, including conditions of crystallization and geochronology. In fact, zircon has become a clue petrogenetic phase due to the well-known zircon crystallization (Ferry and Watson, 2007; Watson et al., 2006) and saturation thermometers (Boehnke et al., 2013; Watson and Harrison, 1983), oxybarometry calibrations (Ballard et al., 2002; Burnham and Berry, 2012; Trail et al., 2011, 2012), its sluggish intracrystalline diffusion rates (Cherniak and Watson, 2007; Cherniak et al., 1997a, 1997b), the high closure temperature of the ^{206}Pb–^{238}U isotopic system (Cherniak and Watson, 2001), the well-known elemental concentrations (Belousova et al., 2002; Hanchar and van Westrenen, 2007; Hoskin and Schaltegger, 2003) and zircon/melt partition coefficients (Fujimaki, 1986; Nagasawa, 1970; Sano et al., 2002; Thomas et al., 2002).

We present LA-ICPMS zircon U–Pb ages of the Upper Cretaceous Caleu pluton of the central Chilean coastal cordillera (Fig. 1a), that cover a wide time interval of zircon crystallization at sample and pluton scale. Because a correct interpretation of the U–Pb zircon ages is crucial to understand the late-stage pluton construction, our efforts will be focused on unraveling the conditions of zircon crystallization by combining zircon geochemistry and whole-rock composition. For this purpose, a numerical solution is developed to estimate the composition and degree of the crystallinity of the zircon crystallizing melts. The plausible mechanisms that reproduce the wide range of zircon ages and temperatures observed at the sample-scale were thermally assessed. Our results lead to a thermal scenario derived from heat transfer by extraction and transportation of melts by diking through a crystal mush (e.g., Bachmann and Bergantz, 2004; Burgisser and Bergantz, 2011; Dufek and Bachmann, 2010; Huber et al., 2009; Miller et al., 2007) during the late pluton growth.

2. The Caleu pluton

The Caleu pluton is located in the easternmost and youngest plutonic belt of the Coastal Batholith of central Chile (~33°S), and belongs to the extensive Early Cretaceous magmatic province of north-central Chile. It roughly corresponds to a medium-grained dioritic to granitic body (Parada et al., 2002, 2005a, 2005b), exhibiting ~1400 m of vertical exposures. It is emplaced into a tilted (30–40°E) and thick volcano-sedimentary succession (Fig. 1a) (Vergara et al., 1995) that includes the Upper Jurassic volcano-sedimentary Horqueta Formation and the following Lower Cretaceous formations: Lo Prado, Veta Negra and Las Chilcas. The western and southwestern margins of the pluton are delimited by fault contacts with the Lo Prado and Veta Negra formations and the La Campana stock, an older (Parada and Larrondo, 1999), small body of medium-grained cumulate gabbro (Molina et al., 2013). The eastern margin is delimited by an intrusive contact with volcanoclastic breccias of the coeval Las Chilcas Formation. A remnant of the roof is preserved in the eastern portion of the pluton, approximately 1200 m lower than the highest peak of the pluton, located in the central part,

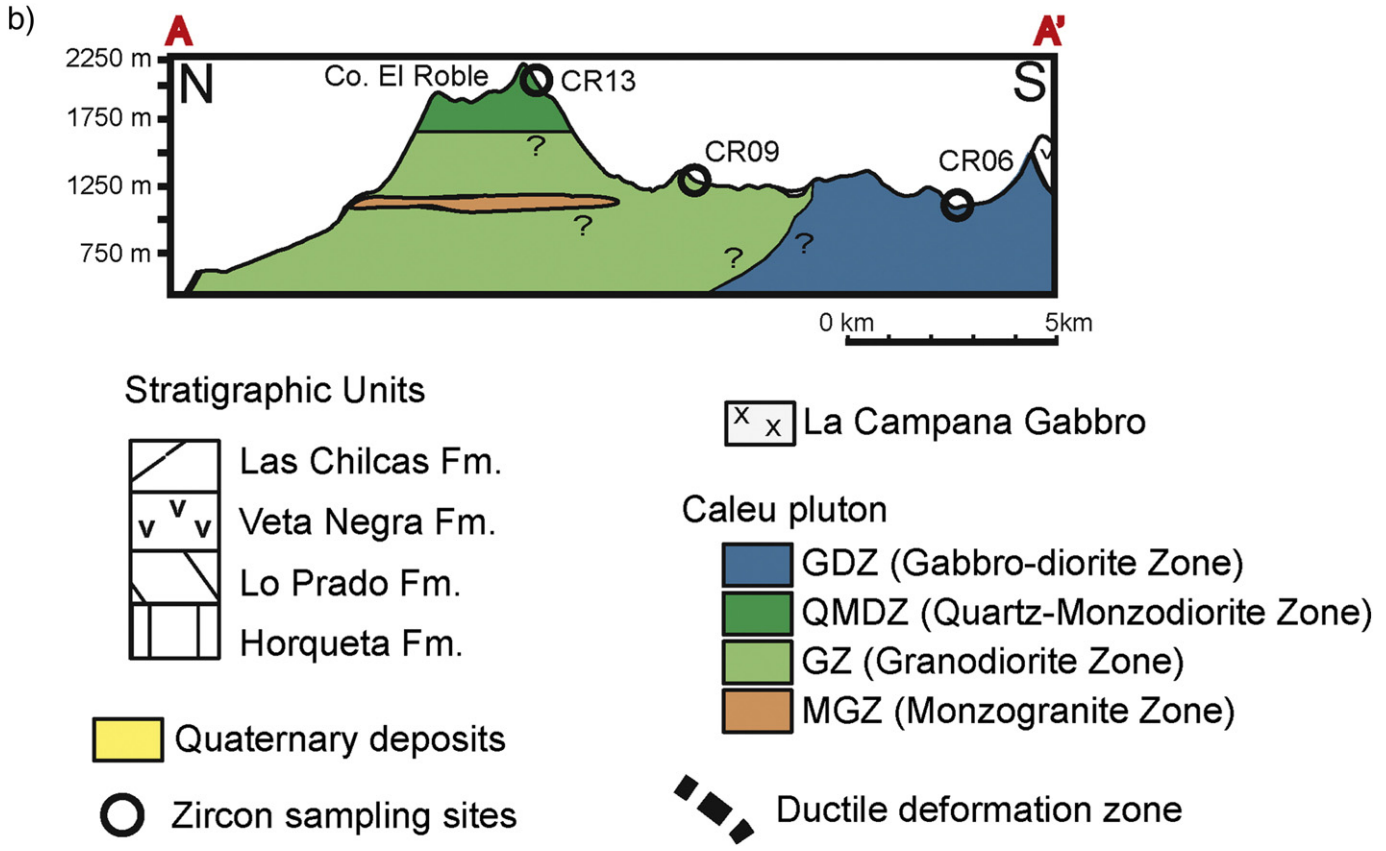

Fig. 1. (a) Geological map of the Caleu pluton consisting of four N–S elongated lithological zones. Circles indicate the zircon age sampling locations. (b) N–S cross-section of the pluton. Inset shows the QAP classification diagram, after Streckeisen (1976), of the four lithological zones of the pluton.
(a) Modified from Parada et al. (2005b).

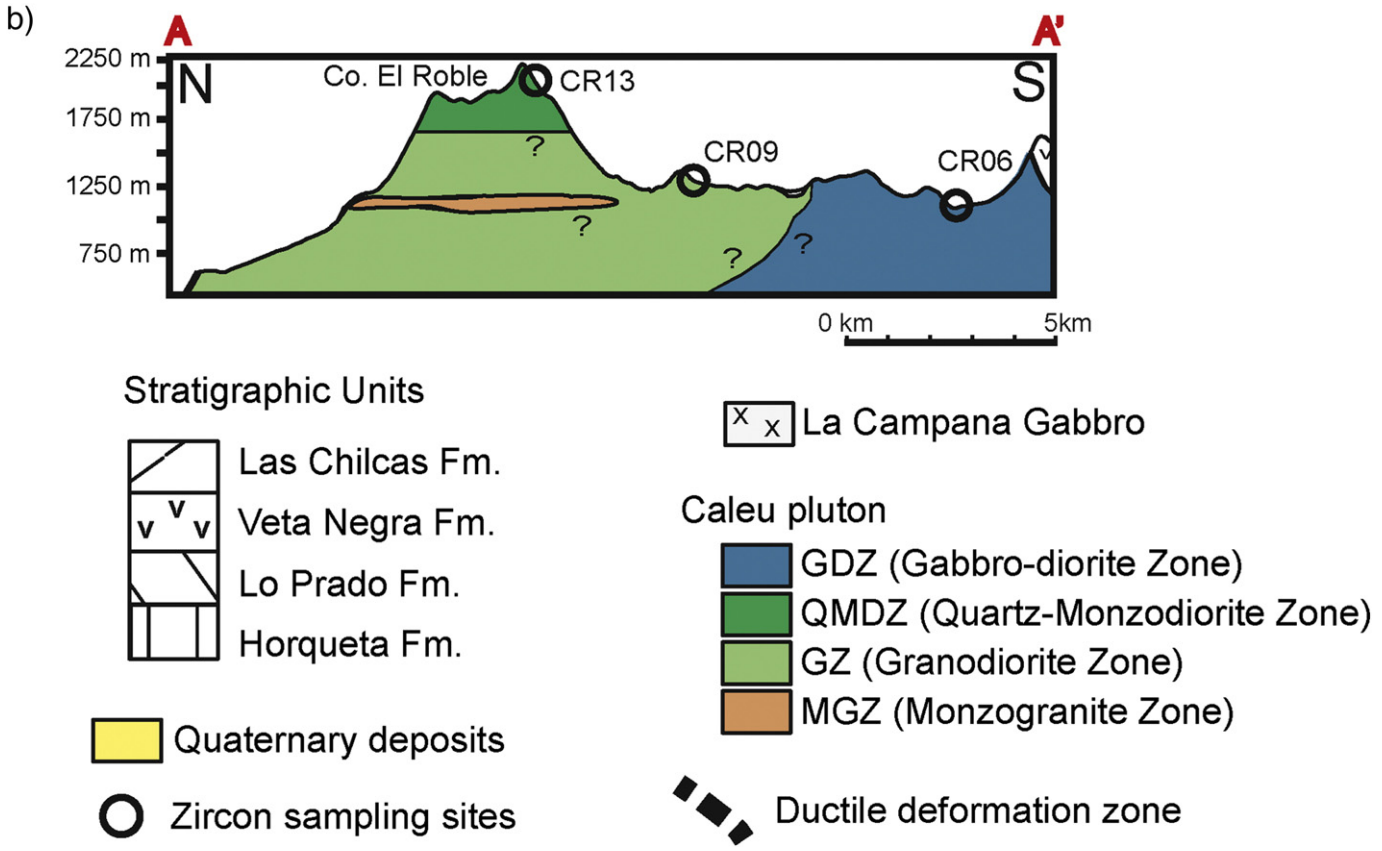

Fig. 1 (*continued*).

suggesting dome-shape geometry, which is consistent with the lobe-like structures defined by magnetic foliations (Parada et al., 2005b). A depth of approximately 7 km (~2 kb) was estimated for the late hornblende crystallization of samples of the upper levels of the intrusion (Parada et al., 2002). Deeper conditions of ≥14 km (≥4 kbar) were estimated from the early magmatic epidote crystallization (Parada et al., 2002).

The Caleu pluton is formed by four N–S elongated lithological zones, covering an area of ~240 km^2: the Gabbro–Diorite Zone (GDZ), the Quartz–Monzodiorite Zone (QMDZ), the Granodiorite Zone (GZ) and the Monzogranite Zone (MGZ) (Fig. 1). The four lithological zones include felsic dikes of variable thickness (0.1–1.0 m) and thin felsic veins (<1.0–3.0 cm). The GDZ primarily occupies an eastern position, totaling ~140 km^2, although there are some outcrops below the GZ of the south-central part of the pluton. The GDZ includes coarse-grained gabbros, diorites and quartz–monzodiorites (51–62 wt.% SiO_2), locally exhibiting ortho- and meso-cumulate oriented plagioclase and subophitic pyroxene and interstitial K-feldspar. The color index varies between 18 and 30. Clinopyroxene, hornblende and biotite are dominant mafic phases and apatite, magnetite, ilmenite, zircon and magmatic epidote are accessory phases. Felsic dikes of approximately 0.25 m thickness are commonly observed (Fig. 3a), as well as centimetric ubiquitous felsic veins (Fig. 3b). The GZ (62–66 wt.% SiO_2) occupies ~62 km^2 of the lower part of the Cerro el Roble (Fig. 1a, b) and consists of fairly homogeneous biotite, amphibole and minor pyroxene granodiorites. Apatite, magnetite, zircon, titanite, and magmatic epidote occur as accessory phases. This lithological zone exhibits a progressive increase in color index and grain size towards the GDZ. Subspheric and rounded microdioritic/gabbroic enclaves ranging from 5 to 70 cm in diameter are locally abundant at the upper part of the GZ, close to the subhorizontal transitional boundary with the QMDZ. Quartz–monzodiorites and minor Quartz–monzonites compose the QMDZ (56–65 wt.% SiO_2), which covers an area of ~8 km^2. Hornblende, biotite and magnetite commonly occur as crystal clots, and clinopyroxene occurs as cores in hornblende crystals. Apatite, magnetite, titanite and zircon are accessory phases. The transition from the GZ to the QMDZ is detailed in a vertical profile below. The MGZ occupies ~30 km^2 to the west of the GZ and consists of hornblende–biotite leucogranodiorites and granites (69–71 wt.% SiO_2). There is an eastward intrusion of a leucogranite sill from the MGZ into the GZ and GDZ (Fig. 1a, b). The modal mineralogy includes medium-grained plagioclase and hornblende phenocrysts as aggregates surrounded by an equigranular intergrowth of fine-grained quartz, K-feldspar, plagioclase, biotite and minor magnetite. Common accessory minerals are magnetite, titanite, zircon and allanite.

A U–Pb age in zircon of 94.2–97.3 Ma was previously determined, concordant with the cooling ages of 94.9 ± 1.8 and 93.2 ± 1.1 Ma obtained from the $^{40}Ar/^{39}Ar$ step-heating plateau ages on amphibole, biotite and plagioclase of the four lithological zones (Parada et al., 2005a), placing the Caleu pluton emplacement and cooling during the transition from a rifted to a compressional regime of the Early Cretaceous continental margin of central Chile (Parada et al., 2005a). Unlike the preceding plutons (Mid-Jurassic and Paleozoic granitoids) and volcanic rocks of the same coastal range segment, the Caleu pluton has the most primitive Sr–Nd isotope composition (εNd between +5.1 and +6.5; Parada et al., 2002, 2005a), implying a MORB-like dominated source, product of the progressive removal of the mantle lithosphere as a result of continuous asthenospheric upwelling during extension (Parada et al., 2005a).

3. Sampling preparation, analytical techniques and procedures

A total of 28 samples collected in a 1 km vertical profile along the Cerro El Roble were crushed and pulverized to at least 95% minus 200 meshes. Subsequently, the samples were mixed with lithium metaborate/tetraborate combined in an induction furnace, then poured into a solution of 5% nitric acid containing an internal standard and mixed continuously until completely dissolved. Major and trace element analyses were obtained using ICP-emission spectrometry and

ICP-MS, respectively, at the Activation Laboratories Lds., Ancaster, Ontario, Canada; FeO values were determined through titration (using potassium dichromate as the tritating agent) via a cold acid digestion of ammonium metavanadate and hydrofluoric acid. Four samples of the Caleu pluton were collected for LA-ICP-MS U–Pb zircon geochronology and geochemistry (Fig. 1a, b): CR06 (diorite from GDZ), CR09 (granodiorite of the GZ), CR13 (quartz–monzodiorite of the QMDZ), and CR15 (monzogranite of the MGZ).

The procedures for zircon separation consisted of sample crushing and grinding followed by zircon concentration via the Wilfley table, magnetic sorting, heavy liquid, and hand picking at the Laboratory of Samples Preparation, Department of Geology, University of Chile. Cathodoluminescence images were acquired for 77 zircon grains, using a Quanta 400 FEG high resolution emission field environmental SEM connected to an Oxford INCA350 EDS and a Gatan Mono CL3 + system with 10 kV imaging conditions and 6.7 nm spot size. U–Pb isotopes and trace elements were simultaneously analyzed at the State Key Laboratory of Geological Processes and Mineral Resources (GPMR), China University of Geosciences, Wuhan, using an Agilent 7500a ICP-MS apparatus coupled with a GeoLas 2005 laser-ablation system with a DUV 193 nm ArF-excimer laser (MicroLas, Germany). Detailed analytical procedures and data reduction are available in Liu et al. (2008, 2010) and are briefly summarized here. A spot size of 32 μm was used for all analyses. Argon was used as the make-up gas and mixed with the carrier gas (helium) via a T-connector before entering the ICP. Nitrogen was added into the central gas flow (Ar + He) of the Ar plasma to decrease the detection limit and improve precision, which increases the sensitivity for most elements by a factor of 2 to 3 (Hu et al., 2008). Each analysis incorporated a background acquisition of 20–30 s (gas blank) followed by 50 s data acquisition. Zircon 91500 was used as a calibration standard for mass discrimination and U–Pb isotope fractionation. The time-dependent drifts of U–Th–Pb isotopic ratios were corrected using a linear interpolation (with time) for every five analyses according to the variations of 91500. The preferred U–Th–Pb isotopic ratios used for 91500 are from Wiedenbeck et al. (1995). The reproducibility of the U–Pb dating with this technique has been evaluated by comparison with the zircon secondary standard GJ-1 (see Supplementary material 1; Jackson et al., 2004). Off-line selection and integration of background and analyzed signals, time-drift correction and quantitative calibration for trace element analyses and U–Pb dating, were performed using ICPMSDataCal (Liu et al., 2008, 2010). The uncertainties of preferred values for the external standard 91500 were propagated into the ultimate results of the samples. Concordia diagrams and weighted mean calculations were made using Isoplot/Ex_ver3 (Ludwig, 2003). Errors associated with individual analyses are quoted at the 1 σ confidence level.

4. Results

4.1. Vertical compositional variations of the upper level of the pluton

The ~1000 m of vertical pluton exposure along the Cerro El Roble (Fig. 1a, b) allowed us to observe the upward lithological and geochemical variations within the pluton (complete whole rock geochemical analyses in Supplementary material 2). Previous studies have detected vertical compositional gradients along this profile, although the compositions of plagioclase and mafic minerals do not substantially vary (Parada et al., 2002, 2005b). Based on a systematic sampling, spaced by approximately 40–70 m in the vertical dimension, we here define a vertical compositional change from the GZ to the QMDZ indicated by a boundary at ~1650 masl (Fig. 2). This boundary is marked by an upward decrease of SiO_2 and Na_2O contents together with an increase, in concentrations and dispersion, of MgO, CaO, Zr, compatible trace element contents (e.g., V and Sc) and $CaO/(Na_2O + K_2O)$ ratios (Fig. 2).

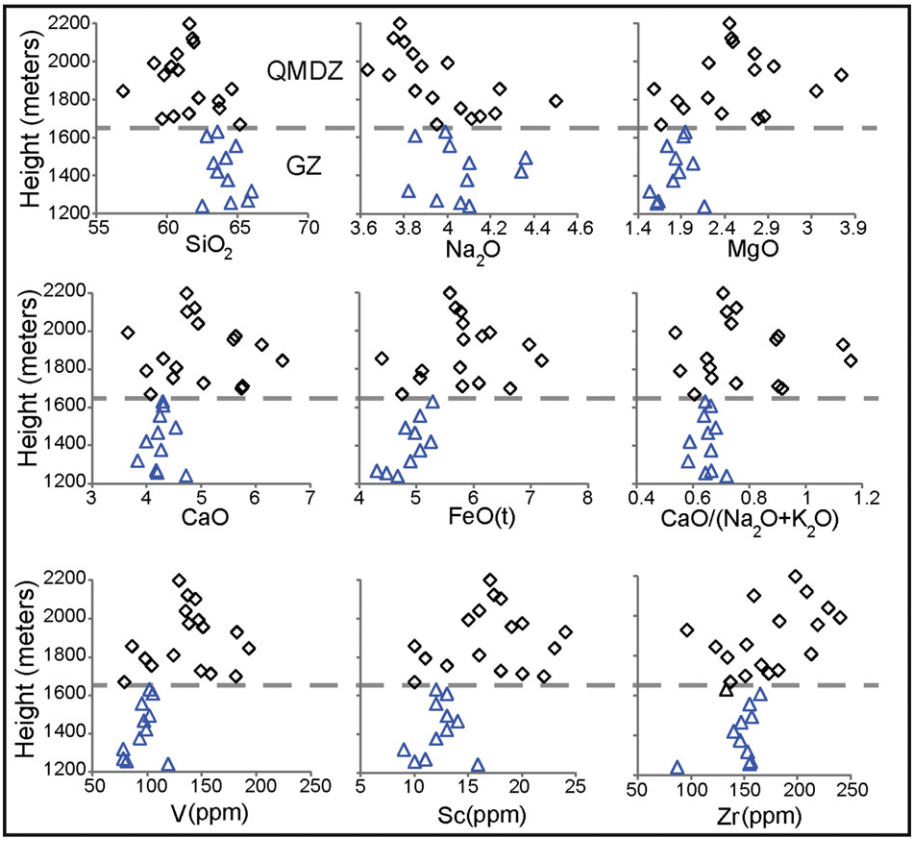

Fig. 2. Vertical whole-rock compositional variations along the N–S cross section shown in Fig. 1b. Dashed line at ~1650 masl defines the compositional boundary between GZ (blue triangles) and QMDZ (black diamonds).

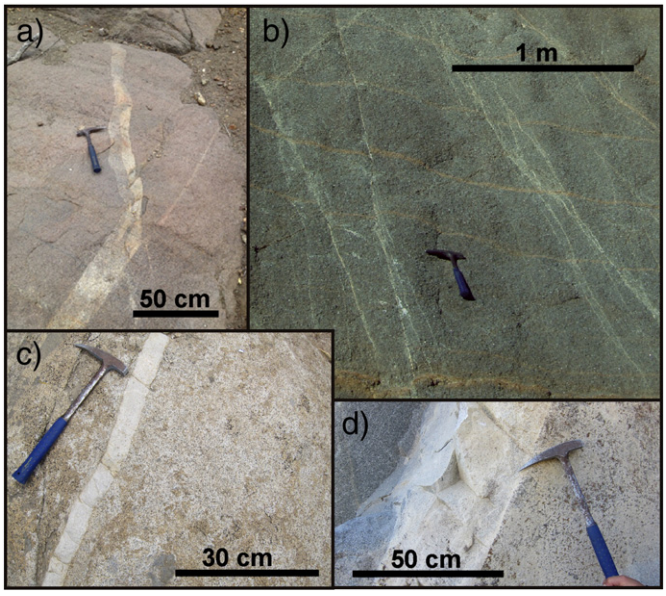

Fig. 3. Granitic felsic dikes and veins of variable thickness hosted in: (a) and (b) GDZ, (c) GZ, and (d) QMDZ.

The exposures of the GZ from 1200 to 1650 masl consist of medium- to coarse-grained biotite–hornblende granodiorites with a color index of approximately 16. Plagioclase crystals are slightly sericitized and commonly surrounded by a mosaic-like intergrowth of quartz and perthitic K-feldspar, and symplectite quartz. Modal content of hornblende and partially chloritized biotite is variable, with Bt/Hbl ratios between 0.5 and 2. These mafic minerals commonly form glomerocrysts (crystal aggregates) with opaques and minor acicular actinolite. Clinopyroxene is the less common (2% modal proportion) mafic mineral [Cpx / (Hb + Bt) = 0.01–0.15; average: 0.06] and is commonly uralitized. Acicular apatite and prismatic zircon are found as accessory phases. Fine-grained microdioritic mafic enclaves are subspheric and rounded, reaching 70 cm in diameter, are ubiquitous along this profile and occur in variable proportions between 4 and 13 enclaves/m^2, reaching their maximum amount at ~1610 masl, close to the compositional boundary with the QMDZ. Granitic dikes and veins of variable thickness (Fig. 3c) from a few centimeters to 50 cm thick occupy approximately 5–10 vol.% of the GZ.

The QMDZ crops out from ~1650 masl to the top of the Cerro el Roble (2200 masl), consisting of medium-grained biotite–hornblende quartz–monzodiorites and quartz–monzonites with a color index similar to the GZ, and more variable Bt/Hb ratios (between 0.13 and 9). Modal contents of up to 8% of the uralitized clinopyroxenes have been detected [Cpx / (Hb + Bt) = 0.06–1.05; average: 0.3]. Glomeroporphyritic aggregates of biotite and amphibole, surrounded by an interstitial graphic intergrowth of perthitic K-feldspar and quartz, are commonly observed. Apatite, magmatic epidote and zircon are found as accessory phases. Aplitic and coarse-grained granitic dikes of ~20–40 cm thick are randomly distributed in the upper part of this zone (Fig. 3d). Elliptic microdioritic enclaves of up to 40 cm long are widely distributed (average 5 enclaves/m^2) but roughly exhibit an upward increase from ~0.25 to ~10 enclaves/m^2. The modal mineralogy of the enclaves primarily consists of abundant plagioclase and minor clinopyroxene and hornblende.

4.2. Zircon morphology

We use the Pupin (1980) typological classification of zircon grains, according to their morphologies and aspect ratios (Fig. 4), which could be attributable to their crystallization conditions and cooling rates (Corfu et al., 2003). GDZ zircon grains correspond to S7, S8 and S9

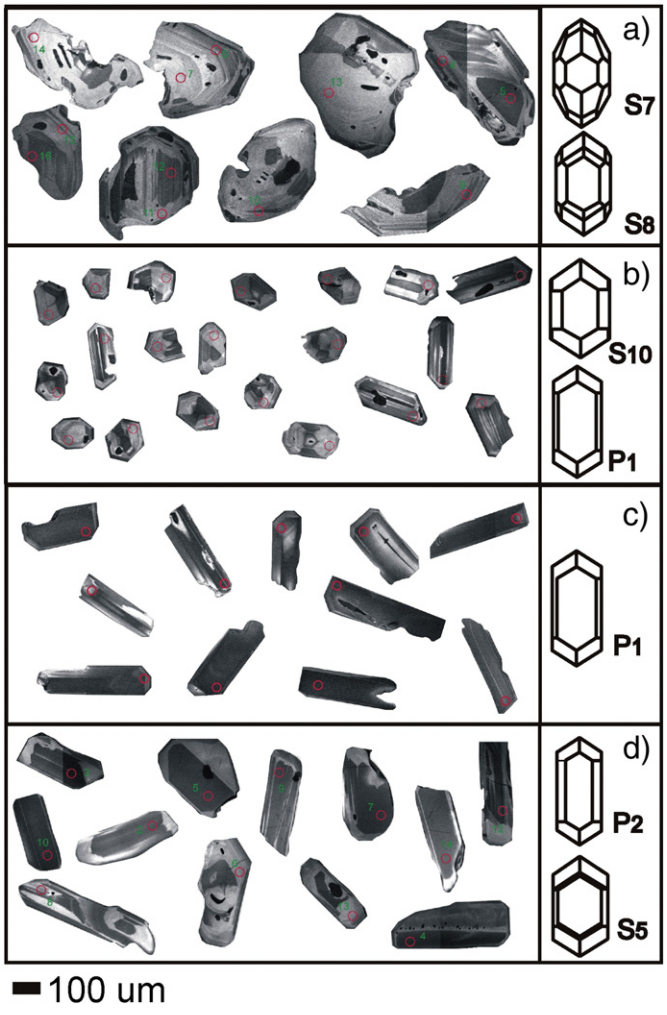

Fig. 4. Cathodoluminescence (CL) images of the analyzed zircon grains of the four Caleu pluton samples. Sites of the U–Pb spot age determinations are shown by red circles. Typological classification according to Pupin (1980) is shown for each zircon sample. (a) GDZ zircon grains exhibit complex zoning, rounded morphologies and resorption features. (b) GZ zircon grains exhibit subtle regular oscillatory zoning and equant aspect ratios. (c) QMDZ zircon grains consist of fairly homogeneous subhedral acicular crystals. (d) Some MGZ zircon grains show well-developed prismatic forms, homogeneous cores and subtle oscillatory zoning.

shapes (Fig. 4a), showing {100} < {110} prismatic forms and a great variety of pyramidal shapes. Cathodoluminescence images show that the size of the analyzed GDZ zircons is slightly variable, being the largest crystals of the studied samples (up to 500 μm) with relatively low aspect ratios. The zircon crystals of the GDZ commonly exhibit complex concentric zoning and rounded shapes, some of them showing discontinuities with internal overgrowths, evidencing multi-stage growth and resorption events (e.g. Gagnevin et al., 2010; Vavra, 1994). These morphologies are similar to those zircon crystals considered as resulting from crystallization from highly fractionated interstitial melts (Corfu et al., 2003). Zircon grains of the GZ samples, classified as S10 and P1 types (Fig. 4b), are the smallest crystals (averaging ~200 μm) found in all studied zircons of the Caleu pluton, exhibiting relatively equant shapes and low aspect ratios, implying very low cooling rates (Corfu et al., 2003). Thin concentric overgrowth rims characterize the GZ zircon grains that differ from the fairly homogeneous tabular zircon crystals of the QMDZ sample. QMDZ zircons exhibit well-preserved subhedral to euhedral shapes with prismatic ({100} < {110}, {100} = {110}) and pyramidal ({101}> > {211}) faces (P1 types, Fig. 4c). QMDZ zircons are commonly unzoned and have the highest aspect ratio of all of the

Table 1
Selected U–Pb LA-ICP-MS data.

	$^{207}Pb/^{235}U$	$^{207}Pb/^{235}U$ (1σ)	$^{206}Pb/^{238}U$	$^{206}Pb/^{238}U$ (1σ)	Rho	$^{206}Pb/^{238}U$ age (Ma)	$^{206}Pb/^{238}U$ error (1σ)
GDZ							
CR-06-01	0.1087	0.0065	0.0158	0.0002	0.2295	101.2	1.38
CR-06-02	0.1111	0.0086	0.0162	0.0003	0.2277	103.5	1.82
CR-06-03	0.1108	0.0062	0.0161	0.0002	0.2603	102.9	1.49
CR-06-04	0.1054	0.0072	0.0151	0.0002	0.2301	96.4	1.51
CR-06-05	0.1122	0.0074	0.0158	0.0003	0.2404	101.3	1.59
CR-06-06	0.1044	0.0045	0.0158	0.0002	0.3009	100.9	1.31
CR-06-07	0.1089	0.0063	0.0160	0.0003	0.2907	102.2	1.71
CR-06-08	0.1125	0.0051	0.0158	0.0002	0.2708	100.8	1.24
CR-06-09	0.1017	0.0047	0.0155	0.0002	0.2526	99.2	1.15
CR-06-10	0.1114	0.0047	0.0152	0.0002	0.2950	97.0	1.20
GZ							
CR-09-01	0.0936	0.0052	0.0148	0.0002	0.1914	94.5	0.99
CR-09-02	0.1015	0.0063	0.0150	0.0002	0.2185	95.8	1.29
CR-09-03	0.1017	0.0058	0.0145	0.0002	0.2382	92.9	1.26
CR-09-04	0.1002	0.0073	0.0148	0.0003	0.2384	94.6	1.64
CR-09-05	0.1028	0.0060	0.0150	0.0002	0.2368	96.0	1.31
CR-09-06	0.1030	0.0063	0.0152	0.0002	0.2543	97.2	1.50
CR-09-07	0.1013	0.0066	0.0154	0.0002	0.2432	98.4	1.56
CR-09-08	0.1028	0.0053	0.0152	0.0002	0.2765	97.2	1.39
CR-09-09	0.1049	0.0049	0.0153	0.0002	0.2699	97.6	1.23
CR-09-10	0.1057	0.0047	0.0152	0.0002	0.3089	97.4	1.34
QMDZ							
CR-13-01	0.0975	0.0041	0.0155	0.0002	0.2885	99.0	1.19
CR-13-02	0.1083	0.0033	0.0152	0.0001	0.2934	97.5	0.87
CR-13-03	0.1049	0.0050	0.0152	0.0002	0.2268	97.1	1.04
CR-13-04	0.1108	0.0084	0.0155	0.0002	0.2125	99.2	1.58
CR-13-05	0.0985	0.0045	0.0154	0.0002	0.2526	98.8	1.14
CR-13-06	0.1016	0.0037	0.0156	0.0001	0.2589	99.6	0.93
CR-13-07	0.1032	0.0036	0.0150	0.0001	0.2477	95.7	0.83
CR-13-08	0.1029	0.0052	0.0147	0.0002	0.2542	94.1	1.20
CR-13-09	0.1013	0.0034	0.0156	0.0001	0.2895	99.6	0.95
CR-13-10	0.1175	0.0046	0.0148	0.0002	0.3301	95.0	1.21
MGZ							
CR-15-01	0.1103	0.0110	0.0151	0.0003	0.2199	96.8	2.10
CR-15-02	0.1059	0.0060	0.0152	0.0002	0.2586	96.9	1.41
CR-15-03	0.1018	0.0055	0.0147	0.0002	0.2381	94.4	1.20
CR-15-04	0.0929	0.0033	0.0146	0.0001	0.2792	93.7	0.93
CR-15-05	0.2507	0.0129	0.0167	0.0003	0.3445	106.7	1.87
CR-15-06	0.1045	0.0067	0.0151	0.0003	0.3234	96.6	2.00
CR-15-07	0.0926	0.0059	0.0146	0.0002	0.2398	93.6	1.43
CR-15-08	0.1068	0.0086	0.0152	0.0003	0.2747	97.0	2.13
CR-15-09	0.1044	0.0073	0.0150	0.0002	0.2310	96.2	1.54
CR-15-10	0.0973	0.0062	0.0149	0.0002	0.2160	95.6	1.31

studied samples which imply a fast magma cooling (Corfu et al., 2003). The morphologies of MGZ zircons correspond to P2 and S5 types (Fig. 4d) and resemble those of the QMDZ zircons but with slightly lower aspect ratios and poorly developed internal zoning and overgrowths. Irrespective of their morphology, most zircon grains form part of a late interstitial quartz–feldspar intergrowth, or as inclusions in late biotite or hornblende.

4.3. Zircon geochronology and geochemistry

$^{206}Pb/^{238}U$ dating on magmatic zircon (selected data in Table 1; complete data list in Supplementary material 2) rims and cores, excluding those discordant ages (less than 10% concordance), indicates relatively clustered ages on the concordia diagram, without significant evidence of inheritance of older grains (Fig. 5a). The weighted average age obtained from the Gaussian distributed MGZ sample ages (MSWD = 0.95; see Fig. 5a) is 94.68 ± 0.71 (2σ confidence), similar to the youngest QMDZ and GZ age clusters, but younger than almost all GDZ ages (Fig. 5b).

Most of the zircon U–Pb ages presented here are consistent with the previous single-grain U–Pb zircon dating of 94.2–97.3 Ma (Parada et al., 2005a, 2005b). Almost all spot ages at sample and pluton scale are substantially overlapped (Fig. 5c), evidencing a protracted zircon crystallization with a subtle decrease of ages from mafic to felsic sample compositions (Fig. 5c).

Selected chemical compositions of zircons of the studied samples are listed in Table 2 (a complete data list is included in Supplementary material 2). All analyzed zircons of the Caleu pluton show the typical REE patterns of unaltered igneous zircons (Hoskin and Schaltegger, 2003), showing an increase of chondrite-normalized element concentrations from La to Lu, and positive Ce and negative Eu anomalies (Fig. 6a). Zircons of the QMDZ sample have the highest total REE contents (Fig. 6b). Ti contents of zircons of the four samples are bracketed between 4.62 and 31.59 ppm.

Th/U ratios of almost all zircons are higher than 0.5 and have a maximum of 1.33 (Table 2), which is indicative of a magmatic origin (Hoskin and Schaltegger, 2003) because metamorphic zircons commonly have Th/U ratios <0.07 (Rubatto, 2002). Zr/Hf ratios of all analyzed zircons of the Caleu pluton are between approximately 36 and 54, and HfO_2 wt.% values are in a restricted range of 0.97–1.69, averaging 1.95, 1.26, 1.23 and 1.2, for the GDZ, GZ, QMDZ and MGZ zircons, respectively. These HfO_2 contents and Zr/Hf ratios are thought to be indicative of late magmatic zircon formation (Wang et al., 2010).

4.4. Zircon crystallization temperatures

To estimate the temperatures of zircon crystallization we use the zircon crystallization thermometer of Ferry and Watson (2007); a proper application of this thermometer requires estimations of the $aTiO_2$ and

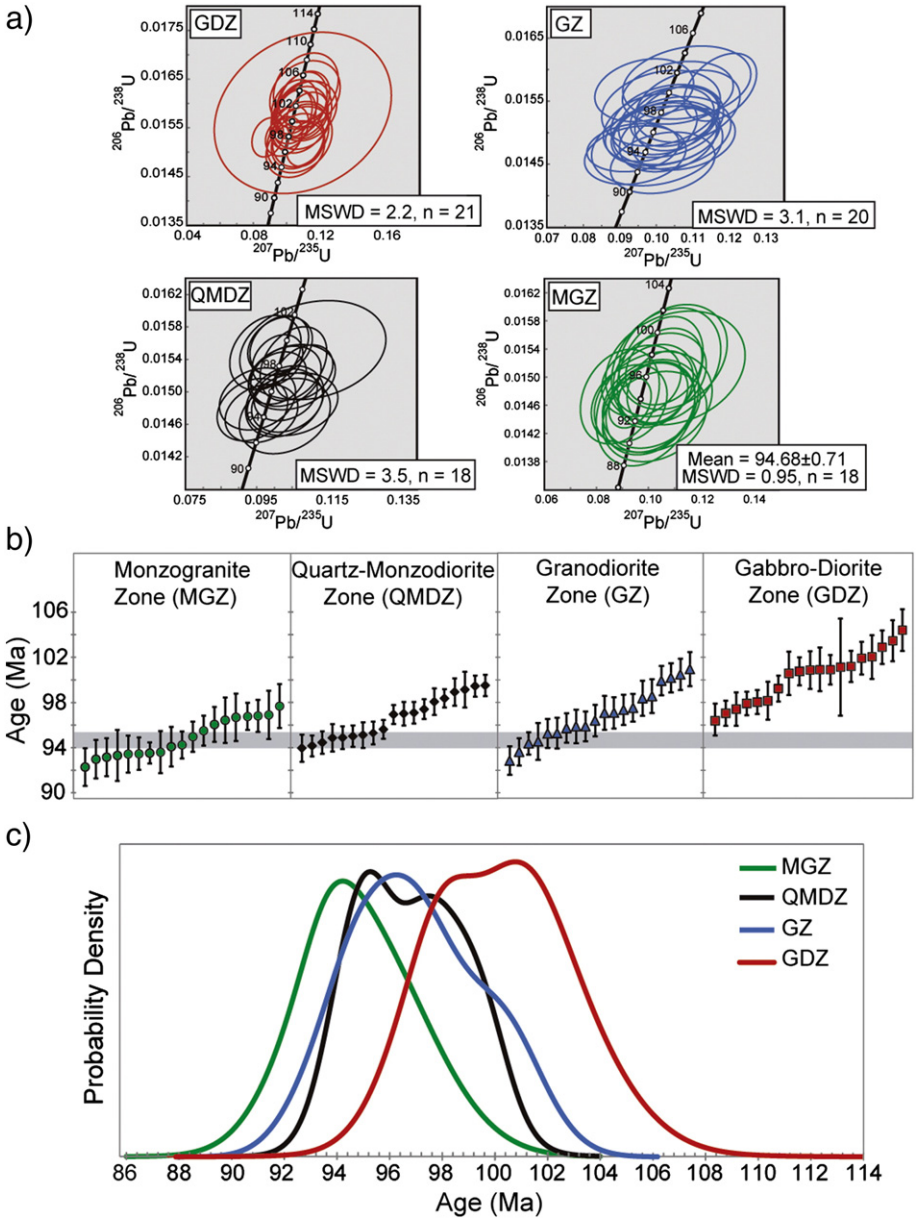

Fig. 5. (a) Concordia diagram plot for each sample, with their respective weighted average and 2σ error. (b) Dates of individual zircon grains of the four lithological zones (error bars at 1σ). Gray rectangle represents the weighted average age of the MGZ zircon sample, at the 2σ confidence level. (c) Probability density plot showing a large overlap and a slight progression towards younger ages, from mafic to felsic sample compositions.

$aSiO_2$ of the melt at time of zircon formation. We consider an $aSiO_2$ of ~1 because quartz is a ubiquitous late magmatic phase in all of the studied samples. Additionally, we estimate an $aTiO_2$ ~ 1 based on the rutile saturation thermometer of Hayden and Watson (2007). The results (see Supplementary material 3) indicate that Ti-bearing phases would have saturated prior to zircon formation (at a slightly higher temperature), resulting in a negligible difference between the zircon crystallization thermometers of Watson and Harrison (1983) and Watson et al. (2006).

Therefore, to calculate the temperatures of the zircon crystallization we use the Watson et al. (2006) calibration, given as:

$$\log(Ti_{Zrn}) = (6.01 \pm 0.03) - {}^{(5080\pm30)}\!/_{T_{cxs}(K)} \quad (1)$$

where Ti_{Zrn} is the titanium concentration (ppm) in zircon, and T_{cxs}(K) the zircon crystallization temperature (uncertainties are quoted at the 2σ level). Most of these temperatures are clustered in the range of 700–850 °C for GDZ, 720–780 °C for the GZ and QMDZ and 750–850 °C for the MGZ zircons (Fig. 7). Zircons from the GDZ sample, which display the widest temperature range of zircon crystallization, exhibit temperatures >800 °C in cores of complexly zoned crystals.

4.5. Composition of the zircon crystallizing melts: a numerical approach

This approach attempts to reproduce the composition of the residual liquid at the zircon crystallization temperatures, using equilibrium crystallization from MELTS software (Asimow and Ghiorso, 1998; Ghiorso and Sack, 1995). This simulation considers the most primitive sample of each lithological zone as initial melt composition, and conditions of 2 kbar (Parada et al., 2002), QFM + 1 and H_2O contents of 0.5, 1.5 and 3.0 wt.% for GDZ, GZ-QMDZ and MGZ, respectively. The Zr (ppm) content of the residual liquids at the onset of zircon crystallization was obtained through the Boehnke et al. (2013) equation:

$$\ln(D_{Zr}) = \frac{10108 \pm 32}{T_{sat}(K)} - (1.16 \pm 0.15)(M-1) - (1.48 \pm 0.09) \quad (2)$$

Table 2
Selected zircon REE and HFSE data (ppm).

	La	Ce	Pr	Nd	Sm	Eu	Gd	Tb	Dy	Ho	Er	Tm	Yb	Lu	Zr	HfO_2 wt.%	Th	U	Th/U
GDZ																			
CR-06-01	0.01	14.85	0.04	0.54	1.48	0.24	9.63	3.59	44.19	18.10	91.65	21.55	215.11	44.50	461,679.86	1.31	129.50	210.20	0.62
CR-06-02	0.00	8.31	0.06	1.25	3.03	0.46	18.59	6.11	74.38	27.27	124.93	26.85	256.33	50.33	458,518.27	1.23	90.95	132.27	0.69
CR-6-03	0.01	10.02	0.06	1.09	2.34	0.23	14.23	5.18	63.83	25.19	121.35	27.34	269.55	56.20	461,112.11	1.25	112.43	196.38	0.57
CR-06-04	0.11	23.31	0.19	3.00	6.62	0.93	35.53	11.26	137.72	52.23	238.76	53.11	504.48	98.62	456,841.39	1.22	358.95	346.78	1.04
CR-06-05	0.02	10.92	0.46	6.70	12.03	1.33	46.98	14.06	161.55	57.62	247.86	50.72	452.10	84.13	468,745.53	1.11	227.55	246.96	0.92
CR-06-06	0.00	13.70	0.06	1.79	3.31	0.40	18.58	6.35	79.16	30.53	144.57	32.77	318.65	64.03	462,669.19	1.27	232.69	327.63	0.71
CR-06-07	0.01	7.55	0.15	2.42	4.82	0.54	23.17	6.99	79.92	29.30	131.94	28.13	265.94	52.41	458,383.22	1.04	98.23	148.26	0.66
CR-06-08	0.00	12.18	0.06	1.05	2.74	0.24	15.52	5.29	65.82	25.81	122.25	27.35	264.86	53.74	464,472.36	1.30	167.68	260.84	0.64
CR-06-09	0.00	12.71	0.02	0.69	2.42	0.21	13.27	4.84	64.47	26.02	128.33	29.89	300.27	60.59	458,196.08	1.40	160.23	302.95	0.53
CR-06-10	0.03	11.21	0.03	1.12	1.92	0.15	11.16	3.86	50.24	19.92	95.24	21.95	219.07	43.99	461,239.16	1.34	133.41	233.47	0.57
GZ																			
CR-09-01	0.01	10.57	0.07	1.35	3.10	0.35	19.16	7.25	92.89	37.76	174.93	38.39	372.19	72.35	8560.89	1.20	164.87	255.98	0.64
CR-09-02	0.00	7.36	0.10	1.74	3.77	0.56	23.16	8.25	101.06	40.59	189.97	41.55	399.27	77.12	7349.24	1.12	109.27	181.54	0.60
CR-09-03	0.00	8.49	0.05	0.82	2.79	0.36	16.78	6.20	78.08	31.37	146.45	32.45	311.82	60.80	6822.45	1.19	110.50	178.46	0.62
CR-09-04	0.03	7.87	0.05	0.47	1.90	0.26	11.57	4.41	58.94	24.16	113.90	25.73	249.20	48.12	6861.88	1.28	83.76	154.15	0.54
CR-09-05	0.01	11.49	0.03	0.87	2.59	0.26	20.97	7.92	102.26	41.59	194.00	42.67	401.54	77.26	9508.87	1.44	149.16	246.21	0.61
CR-09-06	0.00	9.26	0.03	0.70	1.91	0.29	14.32	5.30	67.58	27.85	131.77	28.96	277.21	54.31	7114.37	1.29	99.49	179.66	0.55
CR-09-07	0.02	9.32	0.03	0.81	2.29	0.29	15.43	5.52	72.58	29.20	136.35	30.63	296.20	57.62	7457.10	1.27	107.76	193.19	0.56
CR-09-08	0.00	9.03	0.03	0.58	2.01	0.20	14.50	4.94	67.99	28.18	129.32	28.83	273.90	55.52	3866.00	1.25	101.44	178.50	0.57
CR-09-09	0.00	9.53	0.03	1.02	2.26	0.29	14.75	5.60	73.51	29.92	140.61	31.10	302.44	59.34	7628.96	1.29	147.27	240.17	0.61
CR-09-10	0.38	10.70	0.22	1.75	2.70	0.37	15.86	5.98	76.31	30.82	145.45	32.04	308.34	60.17	7391.04	1.27	119.60	201.77	0.59
QMDZ																			
CR-13-01	0.10	23.11	0.61	9.25	17.91	2.65	133.14	45.59	556.38	213.41	915.94	179.14	1553.61	294.68	453,788.30	1.07	1037.14	778.29	1.33
CR-13-02	0.02	21.79	0.10	2.12	5.40	0.52	34.21	12.65	157.66	63.52	289.89	61.35	559.86	106.78	461,192.79	1.35	650.64	628.33	1.04
CR-13-03	0.01	20.15	0.20	3.50	8.30	1.12	54.38	19.07	232.85	89.73	399.79	81.35	726.84	137.90	464,593.44	1.14	544.02	483.79	1.12
CR-13-04	0.00	11.51	0.16	3.05	7.78	1.06	45.18	15.47	185.61	71.40	309.72	62.82	558.30	106.63	442,520.84	1.23	243.25	290.16	0.84
CR-13-05	0.00	8.14	0.04	0.84	2.82	0.34	17.45	6.23	82.89	33.16	157.96	34.71	339.59	69.39	458,331.97	1.48	99.05	419.40	0.24
CR-13-06	0.03	21.44	0.30	4.92	11.07	1.27	63.08	22.32	277.83	110.08	490.40	99.57	884.08	167.46	461,804.23	1.23	632.80	599.00	1.06
CR-13-07	0.03	17.94	0.17	3.32	7.73	0.83	44.40	15.97	199.08	78.97	355.24	73.82	667.43	127.18	463,825.74	1.33	495.87	532.77	0.93
CR-13-08	0.02	11.37	0.12	3.15	7.83	0.95	44.45	15.09	180.80	68.25	298.48	60.87	542.96	102.54	464,729.71	1.27	223.79	264.92	0.84
CR-13-09	0.04	24.32	0.44	8.41	17.30	1.76	101.46	34.49	414.51	159.24	688.00	136.70	1202.03	221.33	458,810.59	1.21	766.96	701.38	1.09
CR-13-10	0.00	16.54	0.20	3.63	8.15	0.93	48.62	16.92	208.00	80.36	358.05	73.08	653.67	123.66	462,217.94	1.26	400.88	433.13	0.93
MGZ																			
CR-15-01	0.00	5.72	0.03	0.63	1.46	0.24	9.98	3.61	48.23	19.41	92.36	20.88	206.82	40.33	465,907.44	1.21	40.18	76.76	0.52
CR-15-02	0.00	8.68	0.33	5.63	9.88	1.06	47.60	15.05	174.45	63.70	272.86	55.17	486.40	88.04	466,275.96	1.08	149.48	164.36	0.91
CR-15-03	0.04	9.38	0.37	6.31	10.80	1.24	53.96	18.01	212.84	79.95	344.65	68.60	603.07	110.87	462,507.83	1.06	205.73	220.64	0.93
CR-15-04	0.05	16.92	0.38	6.65	12.56	1.20	72.24	24.74	299.42	115.65	498.93	99.75	872.60	160.60	460,868.67	1.17	550.45	529.52	1.04
CR-15-05	0.00	7.21	0.10	2.26	5.92	0.88	32.69	10.62	121.05	45.18	193.19	40.02	366.56	67.75	464,247.65	1.15	92.32	110.47	0.84
CR-15-06	0.00	7.16	0.02	0.70	1.61	0.26	12.64	4.78	62.67	25.23	118.25	26.31	249.75	48.21	463,317.28	1.24	60.63	99.35	0.61
CR-15-07	0.05	7.86	0.41	5.99	9.89	1.15	44.69	13.95	162.76	59.93	257.37	51.13	448.63	82.96	464,361.58	1.07	131.38	166.48	0.79
CR-15-08	0.00	5.29	0.03	0.76	2.21	0.35	14.30	5.13	62.32	23.86	108.96	23.23	218.47	41.65	465,611.03	1.21	45.08	71.67	0.63
CR-15-09	0.03	8.84	0.25	4.51	8.22	0.80	38.82	12.16	138.76	50.44	216.70	43.83	396.14	72.59	464,206.71	1.17	110.08	137.04	0.80
CR-15-10	0.03	11.37	0.19	4.14	9.88	0.82	47.55	15.31	175.65	63.79	273.35	54.55	475.51	85.91	462,634.24	1.23	175.19	218.39	0.80
CR-15-11	0.01	11.54	0.04	0.86	2.69	0.15	17.64	6.64	83.76	32.46	148.73	31.98	302.91	56.61	460,505.21	1.36	128.26	223.89	0.57
CR-15-12	0.04	7.46	0.16	2.94	6.92	1.02	38.54	12.81	152.16	57.00	249.54	51.12	455.44	84.76	462,612.00	1.11	142.69	159.32	0.90
CR-15-13	0.02	7.18	0.03	0.29	1.58	0.16	9.43	3.66	47.55	19.73	93.83	20.48	199.05	38.56	464,123.88	1.30	54.83	104.89	0.52
CR-15-14	0.00	7.33	0.06	2.13	5.22	0.78	28.97	9.45	107.75	39.51	171.21	35.70	321.96	59.82	465,585.11	1.15	94.15	103.91	0.91
CR-15-15	0.00	6.18	0.03	0.28	1.09	0.23	7.66	2.68	36.74	14.96	72.64	16.48	167.30	34.29	457,797.85	1.22	47.09	83.29	0.57
CR-15-16	0.00	7.52	0.02	0.62	1.31	0.22	10.60	4.00	51.52	21.39	99.03	21.74	211.52	40.97	466,195.20	1.32	60.84	118.74	0.51
CR-15-17	0.00	6.81	0.03	0.81	1.99	0.31	14.02	4.83	60.49	23.61	106.98	23.02	217.94	42.20	465,056.90	1.18	56.07	90.86	0.62
CR-15-18	0.00	5.34	0.01	0.54	1.31	0.23	8.31	2.96	38.61	15.87	76.21	17.19	169.84	33.44	466,452.21	1.16	39.75	74.17	0.54
CR-15-19	0.00	13.61	0.04	0.57	2.04	0.09	13.27	5.39	73.89	30.64	152.75	35.03	340.09	67.27	458,920.67	1.69	192.85	420.82	0.46
CR-15-20	0.02	5.75	0.05	0.96	3.08	0.36	14.99	5.11	62.69	23.91	108.18	23.91	227.34	44.08	465,610.54	1.08	55.35	86.45	0.64

where D_{Zr} is the distribution coefficient of Zr between zircon and melt, T_{sat} (K) the zircon saturation temperature of the melt, $M = (Na + K + 2Ca)/(Al * Si)$ is a parameter inversely correlated with peraluminosity and SiO_2 content of the melt. The M values were obtained directly from the MELTS simulation, and Zr concentration in the residual melt is obtained from Eq. (2), assuming that the T_{sat} corresponds to the maximum temperatures of zircon crystallization (T_{cxs}) of the studied samples.

Once the changes in major element composition, mineral phases and crystallinity that undergone the residual melts up to the onset of zircon formation were obtained, the Zr distribution between melt and major crystallizing silicates was iteratively calculated from a mass distribution approach. The Zr concentration in the residual melt, at any moment of the magmatic evolution can be obtained by:

$$\left(C^{Zr}_{melt}\right)_{n+1} = \frac{\left(m^{Zr}_{melt}\right)_n - \sum_{i=1}^{N} Kd_i^{Zr} \times \left(C^{Zr}_{melt}\right)_n \times (\delta G_i)_n}{(MASS_{melt})_{n+1}} \quad (3)$$

where $(C^{Zr}_{melt})_{n+1}$ is the Zr concentration in the melt at the $n + 1$ temperature step, $(m^{Zr}_{melt})_n$ is the mass of Zr in the melt at the n step, $\sum_{i=1}^{N} Kd_i^{Zr} \times (C^{Zr}_{melt})_n \times (\delta G_i)_n$ gives the total Zr mass incorporated in the solid phase, and $(MASS_{melt})_{n+1}$ is the total mass of the residual

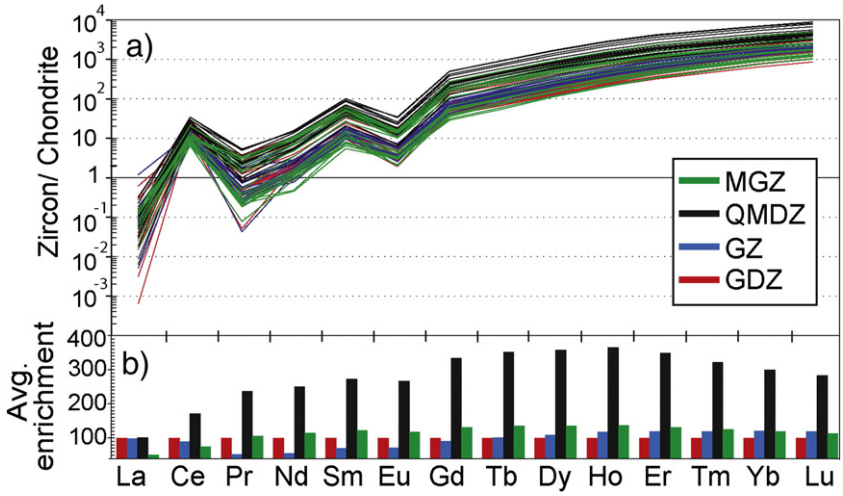

Fig. 6. (a) Chondrite-normalized REE composition of zircons of the Caleu pluton. (b) Average enrichment of REE content of the GZ, QMDZ and MGZ zircons normalized to the average REE content of GDZ zircons. Note that QMDZ zircons have the highest REE contents of the analyzed zircons.

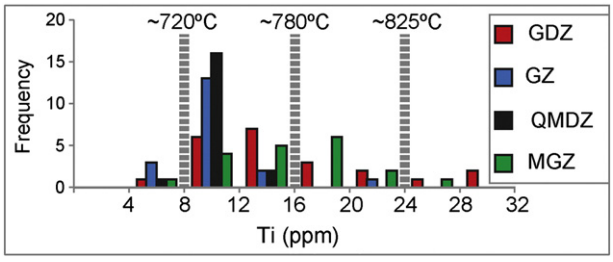

Fig. 7. Frequency histogram of the Ti content of zircons of each sample. Temperatures of zircon crystallization at the corresponding Ti content are indicated as vertical dashed line.

melt (see Appendix A for details). A summary of the results obtained at the onset of zircon crystallization is given in Table 3.

The GDZ, GZ and QMDZ zircons would have been derived from a melt compositionally similar to the MGZ (Fig. 8). The onset of these zircon crystallization takes place after a high crystallinity is reached (Fig. 8) even if high initial H_2O content of the magma is considered. In fact, simulations provided here indicate that the initial H_2O content does not substantially affect the magma crystallinity at the temperature of zircon crystallization (see Supplementary material 4). For example, a crystallinity of >60% is obtained for the GDZ sample with initial H_2O content as high as 3 wt.% (Fig. 9). MGZ zircons would have crystallized from a more Zr-depleted magma with up 30% crystallinity (Fig. 8), probably as a consequence of crystallization of Zr-bearing silicates (amphibole and/or titanite; Bea et al., 2006).

4.6. Origin of the studied zircons: a discussion

The presence of zircons with zoned and partially resorbed cores could indicate an antecrystic origin by for example, multiple stages of crystallization and/or entrainment of zircons formed in deeper levels of the magmatic system (e.g. Schoene et al., 2012). Considering that an efficient transportation of zircons could have been impeded to some extent by the high crystallinity of the hosting magmas (see Fig. 8 and Supplementary material 4), some of the zircons could form in situ, particularly those exhibiting homogeneous and well-developed prismatic forms (e.g. MGZ zircons). Whichever the place where zircons formed they result from crystallization residual melts of similar composition (Fig. 6). The Hf–Ti trend of zircons is used here as a monitor of differentiation, because Hf concentrates in the residual melt (Claiborne et al., 2010b) and Ti is a temperature proxy (Watson et al., 2006). The similar and overlapped Hf–Ti compositional trends (Fig. 10a), observed in zircons of samples of the different zones, indicate that they were probably formed from liquid batches (MGZ-type residual melts) at different evolving stages of the pluton (e.g. Wotzlaw et al., 2013). Consequently, the absence of relationships between zircon composition and age (Fig. 10b) is also indicative of zircon crystallization from non-homogenized batches.

The favorable thermal scenarios that account for the studied zircon crystallization are discussed below.

Table 3
Zircon crystallization conditions of each sample.

	GDZ	GZ	QMDZ	MGZ
Crystallization temperature (°C)	803 °C	811 °C	782 °C	826 °C
Crystallinity	89%	66%	71%	32%
SiO_2 (wt.%)	69%	71%	70%	75%
Zr (ppm)	332	356	271	270
M value	1.55	1.55	1.54	1.2
Initial H_2O (wt.%)	0.5	1.5	1.5	2

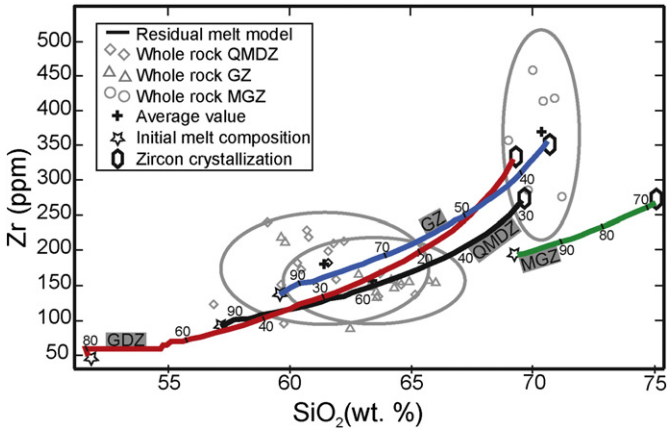

Fig. 8. Calculated composition of the zircon crystallizing melts obtained from the equilibrium crystallization for each lithological unit (see text and Appendix A). Ellipses enclose the whole-rock composition of GZ, QMDZ and MGZ defined at 2σ from the average value of SiO_2 and Zr contents of the respective zone. Numbers above tick marks on the calculated residual liquid line represent the fraction of the remaining melt.
Data from Parada et al. (2002) and this study.

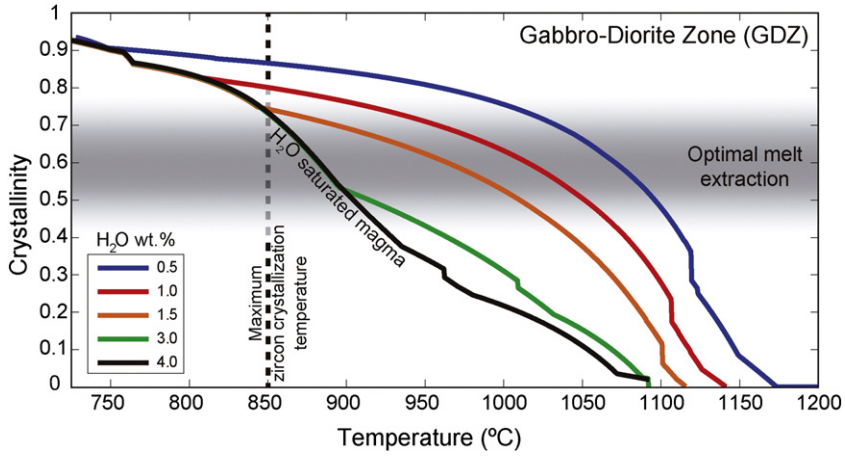

Fig. 9. Variation of crystallinity with temperature upon cooling of an initial melt (equivalent to the composition of most primitive sample of GDZ) with different initial H_2O contents. Curves were obtained by MELTS and the band of crystallinity for the optimal extraction melt is defined according to the proposal of Dufek and Bachmann (2010). Vertical dashed line represents the maximum zircon crystallization temperature recorded for GDZ zircons.

5. Time-dependent thermal modeling for the protracted late stage zircon crystallization

Considering that the capacity of preserving residual melts strongly depends on the mechanism of reservoir construction (e.g., Annen, 2011; Costa, 2008; Gelman et al., 2013b; Glazner et al., 2004; Gutiérrez et al., 2013; Tappa et al., 2011), the large range of zircon crystallization temperatures and ages recorded in each sample (Fig. 11) impose the question about the processes that allow preserving zircon crystallizing melt temperatures for long time intervals. We develop finite element-based simulations using COMSOL Multiphysics® to assess two thermal scenarios derived from: i) a reservoir formed by pulses assembled incrementally and ii) an upward heat transportation of residual melts by successive diking through a crystalline mush. The two scenarios were tested by considering the largest interval of temperature of crystallization and the smallest time range of spot U–Pb ages of zircons at sample scale (GDZ sample: 185 °C, 1.3 Myr; GZ sample: 180 °C, 2.6 Myr and QMDZ sample: 100 °C, 1.6 Myr.; see inset in Fig. 11). The MGZ sample was excluded because its zircon ages are fully overlapped.

5.1. Basis and initial conditions

The simulations provided here take into account the main factors controlling the thermal evolution of a magma system such as the initial temperature of the magma, latent heat of the crystallizing phases, within-reservoir convection, depth of emplacement, thermal gradient before intrusion and nature of the country rocks (Annen et al., 2006; Annen, 2011; Gelman et al., 2013b; see Supplementary material 5). A

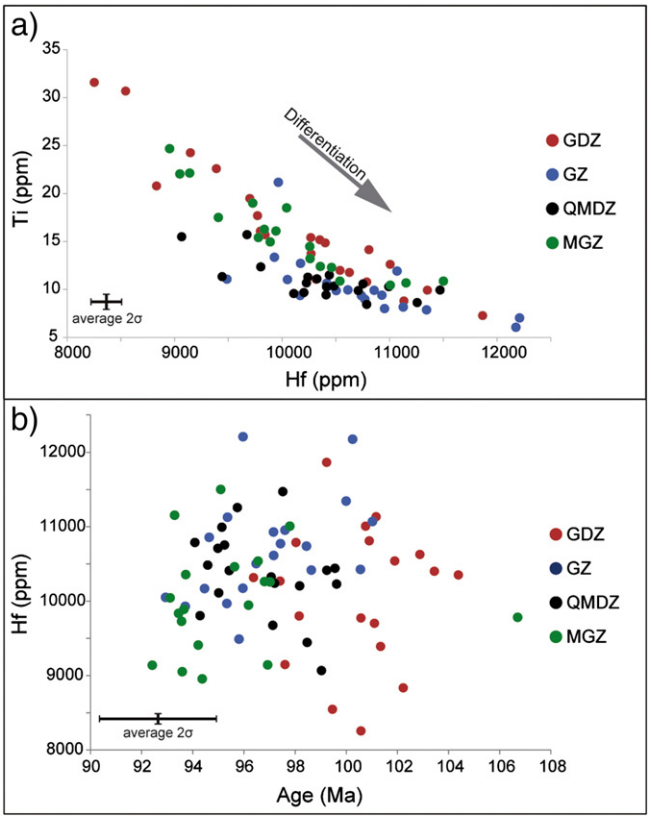

Fig. 10. (a) Ti–Hf plot of zircons of the selected samples showing similar and overlapped trends. Arrows roughly indicate the predicted direction of zircon composition upon differentiation. (b) Scattered Hf-age plot of the studied zircons. The degree of differentiation of the zircon-crystallizing melt appears to be uncoupled with age (see text).

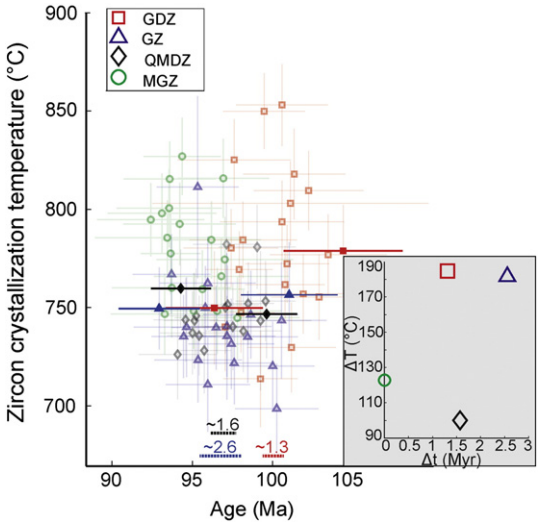

Fig. 11. Temperature of zircon crystallization versus the respective zircon spot age (most data as faded colors). Error bars represent the 2σ confidence intervals. Discontinuous lines represent the minimum U–Pb spot age interval (numbers above each line) between the oldest age and the youngest zircon age (enlightened colors) for each sample, within errors. Inset shows the maximum zircon crystallization temperature interval in each sample versus the minimum age interval.

simple conductive thermal model approach is considered because of the lack of constrains of magma flux inputs in the Caleu pluton and a detailed geometry of the reservoir. The modeled Caleu pluton reservoir has a cylindrical shape where each lithological zone was represented as a geochemically distinct body (see Supplementary material 5). The simulations are constrained by the time and temperature intervals provided by zircons and consider the sample location with respect to the margins of the modeled pluton (ca. 1000 m, 830 m, 0 m and 730 m below the roof; for the GDZ, GZ, QMDZ and MGZ samples, respectively), because cooling at the proximity of the reservoir borders is faster than at the interior.

A reservoir thickness of approximately 7 km was estimated from the pressure conditions of late hornblende (~2 kbar) and early magmatic epidote (~4 kbar) crystallization (Parada et al., 2002). Heat transfer in a flowing magma that includes latent heat of the crystallizing phases is obtained from Gutiérrez and Parada (2010):

$$\rho Cp\frac{\partial T}{\partial t}+\rho Cp\,\vec{u}\cdot\nabla T=\nabla(k\nabla T)+\rho L\frac{\partial X}{\partial T}\frac{\partial T}{\partial t} \quad (4)$$

where ρ is the density, Cp is the heat capacity, T is the temperature, t is the time, u is the magma velocity, L is the latent heat, k is the heat conductivity and X is the exsolved phase fraction. Density, heat capacity and the phase fraction were calibrated with temperature by using MELTS software (Ghiorso and Sack, 1995). Initial compositions equivalent to the whole-rock geochemistry of the sample with the lowest silica content of each lithological zone (Supplementary material 5) were selected. An initial reservoir temperature of 1174 °C, which corresponds to the liquidus temperature of the GDZ given by MELTS, was assumed. Oxygen fugacity conditions of the QFM + 1 buffer were considered.

Temperature-dependent heat conductivity is considered following the thermal diffusivity of Whittington et al. (2009). We use a high latent heat of the cooling magma consistent with the observed high modal abundance (10 vol.%) of magnetite, which has a latent heat as high as 650 kJ/kg (see Supplementary material 5 for details). The magma velocity $\vec{u}$ is obtained by using the incompressible Navier–Stokes formulation:

$$\rho_m\left(\frac{\partial\vec{u}}{\partial t}+\left(\vec{u}\cdot\nabla\right)\vec{u}\right)=\nabla\cdot\left(\mu\left(\nabla\vec{u}+\nabla\vec{u}'\right)\right)-\nabla p-\rho_m\vec{g} \quad (5)$$

$$\nabla\vec{u}=0 \quad (6)$$

where ρ_m is the magma density, $\vec{g}$ is the gravity acceleration vector, $\vec{u}$ is the liquid velocity, p is the pressure, and μ is the dynamic viscosity (density and viscosity were calibrated by MELTS software).

5.2. Conductive thermal model for magma pulses assembled incrementally

Because the cooling rate of the magma body strongly depends on the thermal conditions of the host rocks before or during pluton construction, the previously estimated geothermal gradient of 45 °C/km prior to the Caleu pluton emplacement (Aguirre et al., 1989) can be substantially increased if incremental emplacement of magma batches takes place, resulting in exceptionally high temperatures of the surrounding country rocks (e.g. Annen et al., 2006; Gelman et al., 2013b). For that reason we performed thermal simulations that consider the reservoir construction by successive sill emplacement (considering sills of 200 m thick emplaced by the downdropping/sill insertion procedure; Gelman et al., 2013b) at different injection rates. A 2D axisymmetric cylindrical geometry of a 10 km thick reservoir with a 10 km radius and a roof depth of 5 km (i.e., similar to the estimated volume of the Caleu pluton) is considered. Because as the emplacement rate increases the time of emplacement decreases and the cooling interval increases, we perform two simulations using low and high emplacement rates of 3.18×10^{-3} km^3/yr and 1.57×10^{-2} km^3/yr, equivalent to a sill accretion velocity (e.g. Annen, 2009) of 1.01×10^{-2} m/yr and 4.99×10^{-2} m/yr, respectively. A low emplacement rate of 3.18×10^{-3} km^3/yr was selected because it represents the minimum conditions that allow preserving a very small amount of melt at the time of the next injection (see Supplementary material 5 for details).

5.2.1. Results

The high and low magma injection rates considered here would lead to a completion of the Caleu reservoir between 0.2 and 1.0 Myr. The simulations indicate that the maximum time interval achieved to preserve the melt above the solidus at the sample sites was ~0.9 and 0.1 Ma, for the high and low magma emplacement rates, respectively. Considering the lowest emplacement rate (3.18×10^{-3} km^3/yr), the minimum thermal condition to preserve melts for the observed 2.6 Myr (just above 0% melt fraction) is numerically reproduced only if an extremely thick magma reservoir is considered (>25 km thick; see Supplementary material 5).

5.3. Thermal model of upward heat redistribution by diking in a mush system

Despite magma pulses assembled incrementally gave maximum intervals for preserving residual melts shorter than the interval of zircon crystallization in geologically reasonable conditions, it cannot be ruled out if it acts together with upward heat transfer by diking. Dufek and Bachmann (2010) numerically demonstrated that residual silicic melts have a high probability to be extracted from a mush of crystallinity between ~50 and 70 vol.%. Thus, if zircons of the GDZ, GZ and QMDZ crystallized from magmas with a crystallinity higher than 60 vol.%, even considering high water content (Fig. 9; Supplementary material 4), efficient melt extraction operates. The exception would be the MGZ zircons that would have crystallized from convective melts.

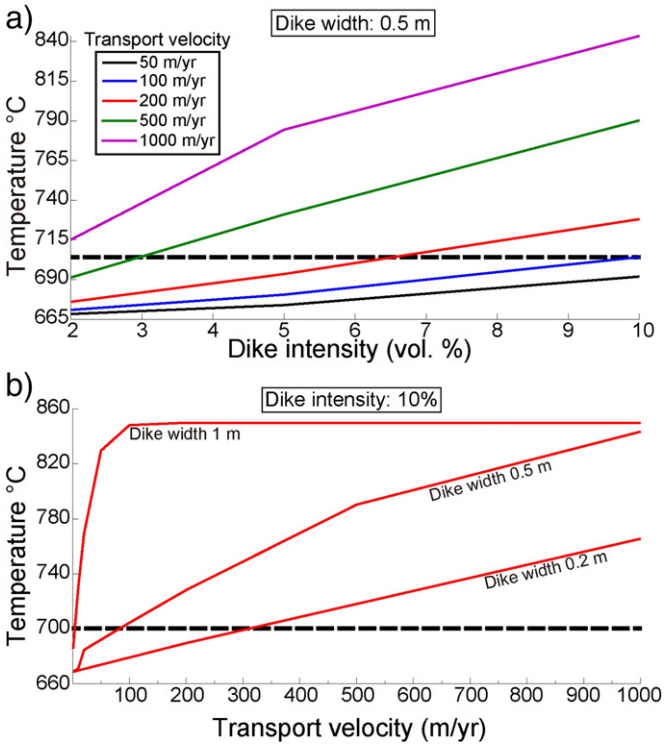

Fig. 12. Thermal model for melt transport by diking: (a) temperatures obtained versus dike intensity, considering a dike width of 0.5 m. (b) Temperature versus transport velocity, considering a dike intensity of 10%. Discontinuous black line indicates the 700 °C isotherm, representing the solidus temperature. Note that reheating above the solidus temperature is strongly favored by high transport velocities regardless of the dike width and intensity.

A simple scenario of continuous upward heat and residual melt redistribution by diking through 2 km thick crystalline mush up to the upper levels of the pluton is thermally modeled. The mentioned upper two kilometers of the system corresponds to the section where a short time interval of residual melt preservation is expected and the samples collected. A longer melt transport from deeper levels of the mush would not substantially affect the simulated heat redistribution (see Supplementary material 5) because the heat of the magma system dissipates roofward. The scenario of residual melt transportation is strongly supported by the abundance of felsic dikes and thin veins hosted in the pluton (Fig. 3) and could explain why the QMDZ (the uppermost lithological zone) exhibits a large dispersion of the whole-rock composition (Fig. 2) and anomalously high incompatible trace element content of zircons (Fig. 6b) with respect to the underlying, more felsic GZ unit.

The influence of the following parameters was evaluated: (i) dike width, (ii) transport velocity and (iii) dike intensity (in the sense of Walker, 1986) expressed in vol.% of dikes and assuming a regularly-spaced distribution. The changing properties of the transported magma (temperature, density and viscosity) were derived from the differentiation of the most primitive GDZ sample using MELTS software. The simulations consider a temperature of 850 °C for the initial mush, and an initial geothermal gradient of 45 °C/km and were performed with dike widths between 20 cm and 1 m, melt transport velocities between 1 m/yr and 1000 m/yr and dike intensities between 2% and 10%. The dike intensity and width of the dikes were inferred from field observations (Fig. 3). Because the dike intensity and thickness are only locally recorded in the field and there is no data of the velocity of dike melt transport, our simulations allowed estimating the melt velocity (see Eqs. (5) and (6)) and its effect on heat redistribution at the upper levels of the Caleu mush system. The results provide the minimum reheating conditions because they do not account for the melt distribution (extraction/injection) between dike and the hosting mush.

5.3.1. Results and discussion

The simulations indicate that higher dike intensities substantially contribute to reheat the mush zone between dikes. For example at 1 km below the top of the pluton, a dike system of 50 cm thick with dike intensities of 2%, 5% and 10%, a minimum magma transport velocity of approximately 700, 300 and 100 m/yr is required, respectively, to maintain the mush temperature higher than 700 °C (Fig. 12a). The thermal effect of the melt transport velocity is also relevant: thin dikes require higher melt transport velocities than thick dikes. For example, for a dike intensity of 10% at 1 km below the roof, a dike system of 20, 50 and 100 cm thick is able to maintain the mush temperature above 700 °C if the transport melt velocities are higher than 300, 100 and 20 m/yr, respectively (Fig. 12b). On the other hand, the amount of melt transferred by diking with respect to the volume of the Caleu pluton strongly depends on melt transport velocity. For example, for dike intensities of 2%, 5% and 10%, and a velocity of 100 m/yr, the amount of redistributed melt during 1 Myr of continuous transport is high, exceeding the volume of the pluton (see Supplementary material 5). Based on the fact that the MGZ sample zircons have fully overlapped spot ages and the assumption that they would have crystallized from a low-crystallinity melt (Fig. 8; Table 3, Supplementary material 4), an origin of the MGZ as a result of the accumulation of transported residual melts is speculated. Because the volume of the MGZ exposures is about 1/8 of the total volume of the pluton and is substantially smaller than the calculated volume of melts under continuous transport, a scenario of melt transportation by diking of successive batches is suggested. Finally, we advocate that the transported melts could come from a rejuvenated mush during the incremental pluton growth (as discussed above) providing melt input from below and explaining small scale heterogeneities (e.g. Burgisser and Bergantz, 2011). Consistent with this are the variable temperatures and ages of zircon crystallization recorded at sample scale (Figs. 7 and 11).

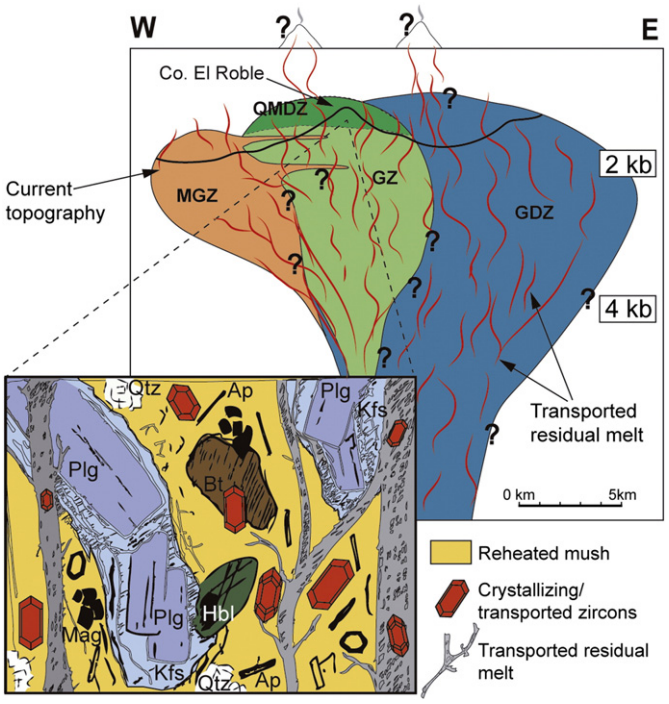

Fig. 13. Conceptual model of the development of the late-magmatic stage of the Caleu pluton. Inset shows the micro-scale mineral development and reheating influence due to transported liquids through veins and dikes. Note that in this conceptual cartoon, dikes and veins transport and redistribute liquids and heat; some dikes could coalesce at the MGZ while others could form part of the volcano-clastic counterpart (Las Chilcas Formation) of the Caleu pluton. Dike width and zircon size are not for scale.

6. Conclusions

Geochronology and geochemistry data of zircons from four samples of the Caleu pluton indicate a large and similar age and temperature interval of zircon crystallization from silicic residual melts, irrespective of the whole-rock composition. A numerical approach indicates that the calculated SiO_2 and Zr (ppm) contents of the zircon crystallizing melts of the GDZ, GZ and QMDZ resemble those of the whole-rock composition of the MGZ. Conductive thermal modeling indicates that the protracted zircon crystallization of up to 2.6 Myr cannot be solely explained by magma pulses assembled incrementally. Upward heat redistribution by melts extracted and transported by dikes through a mush is an efficient mechanism to preserve the magma system above solidus temperature for a long time (Fig. 13). This scenario is supported by the abundance of felsic dikes hosted in the pluton and is consistent with the anomalously high incompatible trace element content of zircons of the uppermost sample, and with the large variability of whole-rock composition exhibited by the QMDZ in the upper part of the pluton. The model of melts transported by diking presented here needs geological explanations to account for the fate of the displaced melts. The MGZ could be a testimony of accumulation of dike-transported silicic melts, and the volcanoclastic breccias (felsic and intermediate composition) of Las Chilcas Formation, deposited coevally with the Caleu pluton emplacement, would represent the removal of the volcanic counterpart of the Caleu pluton. In fact, Las Chilcas Formation is thought to represent a syntectonic molasse derived from the rapid exhumation of the Caleu pluton that started nearly coeval with its emplacement (Parada et al., 2005a). It is interesting to note that a large U–Pb zircon spot age dispersion at the sample scale does not necessary derive from analytical uncertainties, but may indicate a geological process of prolonged events of zircon crystallization as it is recognized in the Caleu pluton.

Acknowledgments

This work was financed by the CONICYT-FONDAP project 15090013 of the Andean Geothermal Centre of Excellence (CEGA), and the M.Sc. CONICYT 221320021 grant. A collaborative work between the University of Chile and China University of Geosciences, Wuhan, is acknowledged. We also thank the anonymous reviewers for their constructive comments, as their suggestions greatly improved the manuscript.

Appendix A

To obtain the zirconium content in the residual melt that lead to zircon crystallization, a numerical iterative approach is presented. The mass distribution between major silicates and the residual melt in the whole range of modeled temperatures were obtained as follows:

The zirconium concentration C_i^{Zr} in any *i* crystalline phase is:

$$C_i^{Zr} = \frac{m_i^{Zr}}{MASS_i} \tag{A1}$$

being m_i^{Zr} the mass of zirconium contained, and $MASS_i$ the total mass of the phase *i*.

The total zirconium mass on the solid phase is:

$$MASS_{solid}^{Zr} = \sum_{i=1}^{N} m_i^{Zr} \tag{A2}$$

and the partition coefficient *Kd* between the melt and a phase *i*:

$$Kd_i^{Zr} = \frac{C_i^{Zr}}{C_{melt}^{Zr}}. \tag{A3}$$

From Eq. (A3) and replacing C_i^{Zr} as shown in Eq. (A1), we obtain the total zirconium mass in *i*:

$$(\boldsymbol{c}) \rightarrow Kd_i^{Zr} \times C_{melt}^{Zr} = C_i^{Zr} \overset{(\boldsymbol{a})}{\rightarrow} Kd_i^{Zr} \times C_{melt}^{Zr} \times MASS_i = m_i^{Zr}. \tag{A4}$$

The total zirconium mass on the solid phase is expressed as function of the partition coefficients Kd_i^{Zr}, the concentration of zirconium in the melt C_{melt}^{Zr}, and the total mass of each crystallizing mineral $MASS_i$, as:

$$MASS_{solid}^{Zr} = \sum_{i=1}^{N} Kd_i^{Zr} \times C_{melt}^{Zr} \times MASS_i. \tag{A5}$$

The mass matrix $G_{(n \times N)}$ is obtained through MELTS software, being *n* the number of modeled temperature steps and *N* the quantity of solid phases in equilibrium with the melt. Similarly $\delta G_{((n-1)\times N)}$ corresponds to the amount of mass entrained in each mineral phase as temperature decrease.

$$G_{(n \times N)} = \begin{bmatrix} MASS_1^1 & \cdots & MASS_N^1 \\ \vdots & \ddots & \vdots \\ MASS_1^n & \cdots & MASS_N^n \end{bmatrix} \rightarrow$$
$$\delta G_{((n-1)\times N)} = \begin{bmatrix} \delta MASS_1^1 & \cdots & \delta MASS_N^1 \\ \vdots & \ddots & \vdots \\ \delta MASS_1^{n-1} & \cdots & \delta MASS_N^{n-1} \end{bmatrix} \tag{A6}$$

Using Eqs. (A5) and (A6), the total zirconium mass entrained in the solid phase, in each step *n*:

$$\delta\left(MASS_{solid}^{Zr}\right)_n = \sum_{i=1}^{N} Kd_i^{Zr} \times \left(C_{melt}^{Zr}\right)_n \times (\delta G_i)_n. \tag{A7}$$

Therefore, changes in the zirconium concentration in the residual melt (Eq. (A3)), as the zirconium mass in the melt $(m_{melt}^{Zr})_n$ minus the total mass of zirconium entrained in solids $-\ \delta(M_{solid}^{Zr})_n$, divided by the total mass of melt after crystallization $(MASS_{melt})_{n+1}$:

$$\left(C_{melt}^{Zr}\right)_{n+1} = \frac{(m_{melt}^{Zr})_n - \delta\left(M_{solid}^{Zr}\right)_n}{(MASS_{melt})_{n+1}} \overset{(g)}{\rightarrow} \frac{(m_{melt}^{Zr})_n - \sum_{i=1}^{N} Kd_i^{Zr} \times \left(C_{melt}^{Zr}\right)_n \times (\delta G_i)_n}{(MASS_{melt})_{n+1}}. \tag{A8}$$

Finally, once the starting zirconium concentration in the melt is calculated through Boehnke's et al. (2013) zircon solubility model (Eq. (2) in the main text), iterating Eqs. (A7) and (A8) (using the MATLAB R2010a software) derives in obtaining the whole range of zirconium concentration $\overrightarrow{\boldsymbol{C}_{\boldsymbol{melt}}^{\boldsymbol{Zr}}}(\boldsymbol{1} \times \boldsymbol{n})$ in every n temperature step.

Appendix B. Supplementary data

Supplementary data to this article can be found online at http://dx.doi.org/10.1016/j.lithos.2015.04.008.

References

Aguirre, L., Levi, B., Nyström, J.O., 1989. The link between metamorphism, volcanism and geotectonic setting during the evolution of the Andes. Geological Society, London, Special Publications 43, 223–232.
Annen, C., 2009. From plutons to magma chambers: thermal constraints on the accumulation of eruptible silicic magma in the upper crust. Earth and Planetary Science Letters 284, 409–416.
Annen, C., 2011. Implications of incremental emplacement of magma bodies for magma differentiation, thermal aureole dimensions and plutonism–volcanism relationships. Tectonophysics 500, 3–10.
Annen, C., Scaillet, B., Sparks, R.S.J., 2006. Thermal constraints on the emplacement rate of a large intrusive complex: the Manaslu Leucogranite, Nepal Himalaya. Journal of Petrology 47, 71–95.
Asimow, P.D., Ghiorso, M.S., 1998. Algorithmic modifications extending MELTS to calculate subsolidus phase relations. American Mineralogist 83, 1127–1131.
Bachmann, O., Bergantz, G.W., 2004. On the origin of crystal-poor rhyolites: extracted from batholithic crystal mushes. Journal of Petrology 45, 1565–1582.
Ballard, J.R., Palin, J.M., Campbell, I.H., 2002. Relative oxidation states of magmas inferred from Ce(IV)/Ce(III) in zircon: application to porphyry copper deposits of northern Chile. Contributions to Mineralogy and Petrology 144, 347–364.
Barboni, M., Schoene, B., Ovtcharova, M., Bussy, F., Schaltegger, E., Gerdes, A., 2013. Timing of incremental pluton construction and magmatic activity in a back-arc setting revealed by ID-TIMS U/Pb and Hf isotopes on complex zircon grains. Chemical Geology 340, 76–93.
Bea, F., Montero, P., Ortega, M., 2006. A LA-ICP-MS evaluation of Zr reservoirs in common crustal rocks: implications for Zr and Hf geochemistry, and zircon-forming processes. The Canadian Mineralogist 44, 693–714.
Belousova, E.A., Griffin, W.L., O'Reilly, Y.O., Fisher, N.I., 2002. Igneous zircon: trace element composition as an indicator of source rock type. Contributions to Mineralogy and Petrology 143, 602–622.
Bergantz, G.W., 2000. On the dynamics of magma mixing by reintrusion: implications for pluton assembly processes. Journal of Structural Geology 22, 1297–1309.
Boehnke, P., Watson, E.B., Trail, D., Harrison, T.M., Schmitt, A.K., 2013. Zircon saturation re-revisited. Chemical Geology 351, 324–334.
Burgisser, A., Bergantz, G.W., 2011. A rapid mechanism to remobilize and homogenize highly crystalline magma bodies. Nature 471, 212–215.
Burnham, A.D., Berry, A.J., 2012. An experimental study of trace element partitioning between zircon and melt as a function of oxygen fugacity. Geochimica et Cosmochimica Acta 95, 196–212.
Cherniak, D.J., Watson, E.B., 2001. Pb diffusion in zircon. Chemical Geology 172, 5–24.
Cherniak, D.J., Watson, E.B., 2007. Ti diffusion in zircon. Chemical Geology 242, 473–486.
Cherniak, D.J., Hanchar, J.M., Watson, E.B., 1997a. Rare-earth diffusion in zircon. Chemical Geology 134, 289–301.
Cherniak, D.J., Hanchar, J.M., Watson, E.B., 1997b. Diffusion of tetravalent cations in zircon. Contributions to Mineralogy and Petrology 127, 383–390.
Claiborne, L.L., Miller, C.F., Flanagan, D.M., Clynne, M.A., Wooden, J.L., 2010a. Zircon reveals protracted magma storage and recycling beneath Mount St. Helens. Geology 38, 1011–1014.
Claiborne, L.L., Miller, C.F., Wooden, J.L., 2010b. Trace element composition of igneous zircon: a thermal and compositional record of the accumulation and evolution of a large silicic batholith, Spirit Mountain, Nevada. Contributions to Mineralogy and Petrology 160, 511–531.
Coleman, D.S., Gray, W., Glazner, A.F., 2004. Rethinking the emplacement and evolution of zoned plutons: geochronologic evidence for incremental assembly of the Tuolumne Intrusive Suite, California. Geology 32, 433–436.
Corfu, F., Hanchar, J.M., Hoskin, P.W.O., Kinny, P., 2003. Atlas of zircon textures. In: Hanchar, J.M., Hoskin, P.W.O. (Eds.), Zircon. Reviews in Mineralogy and Geochemistry. Mineralogical Society of America 53, pp. 469–500.
Costa, F., 2008. Residence times of silicic magmas associated with calderas. In: Gottsmann, J., Marti, J. (Eds.), Caldera Volcanism: Analysis, Modelling and Response: Developments in Volcanology. vol. 10. Elsevier, Amsterdam, pp. 1–55.

Díaz Alvarado, J., Fernández, C., Castro, A., Moreno-Ventas, I., 2013. SHRIMP U–Pb zircon geochronology and thermal modeling of multilayer granitoid intrusions. Implications for the building and thermal evolution of the Central System batholith, Iberian Massif, Spain. Lithos 175–176, 104–123.
Dufek, J., Bachmann, O., 2010. Quantum magmatism: magmatic compositional gaps generated by melt-crystal dynamics. Geology 38, 687–690.
Ferry, J.M., Watson, E.B., 2007. New thermodynamic models and revised calibrations for the Ti-in-zircon and Zr-in-rutile thermometers. Contributions to Mineralogy and Petrology 154, 429–437.
Fujimaki, H., 1986. Partition coefficients of Hf, Zr, and REE between zircon, apatite, and liquid. Contributions to Mineralogy and Petrology 94, 42–45.
Gagnevin, D., Daly, J.S., Kronz, A., 2010. Zircon texture and chemical composition as a guide to magmatic processes and mixing in a granitic environment and coeval volcanic system. Contributions to Mineralogy and Petrology 159, 579–596.
Gelman, S.E., Deering, C.D., Gutiérrez, F.J., Bachmann, O., 2013a. Evolution of the Taupo Volcanic Center, New Zealand: petrological and thermal constraints from the Omega dacite. Contributions to Mineralogy and Petrology 166, 1355–1374.
Gelman, S.E., Gutiérrez, F.J., Bachmann, O., 2013b. On the longevity of large upper crustal silicic magma reservoirs. Geology 41, 759–762.
Ghiorso, M.S., Sack, R.O., 1995. Chemical mass transfer in magmatic processes IV. A revised and internally consistent thermodynamic model for the interpolation and extrapolation of liquid–solid equilibria in magmatic systems at elevated temperatures and pressures. Contributions to Mineralogy and Petrology 119, 197–212.
Glazner, A.F., Bartley, J.M., Coleman, D.S., Gray, W., Taylor, R.Z., 2004. Are plutons assembled over millions of years by amalgamation from small magma chambers? GSA Today 14, 4–11.
Gutiérrez, F.J., Parada, M.A., 2010. Numerical modeling of time-dependent fluid dynamics and differentiation of a shallow basaltic magma chamber. Journal of Petrology 513, 731–762.
Gutiérrez, F.J., Payacan, I., Gelman, S.E., Bachmann, O., Parada, M.A., 2013. Late-stage magma flow in a shallow felsic reservoir: merging the anisotropy of magnetic susceptibility record with numerical simulations in La Gloria Pluton, central Chile. Journal of Geophysical Research, Solid Earth 118, 1–15.
Hanchar, J.M., van Westrenen, W., 2007. Rare earth element behavior in zircon-melt systems. Elements 3, 37–42.
Hayden, L.A., Watson, E.B., 2007. Rutile saturation in hydrous siliceous melts and its bearing on Ti-thermometry of quartz and zircon. Earth and Planetary Science Letters 258, 561–568.
Hoskin, P.W.O., Schaltegger, U., 2003. The composition of zircon and igneous and metamorphic petrogenesis. In: Hanchar, J.M., Hoskin, P.W.O. (Eds.), Zircon. Reviews in Mineralogy and Geochemistry. Mineralogical Society of America 53, pp. 27–62.
Hu, Z.C., Gao, S., Liu, Y.S., Hu, S.H., Chen, H.H., Yuan, H.L., 2008. Signal enhancement in laser ablation ICP-MS by addition of nitrogen in the central channel gas. Journal of Analytical Atomic Spectrometry 23, 1093–1101.
Huber, C., Bachman, O., Manga, M., 2009. Homogenization processes in silicic magma chambers by stirring and mushification (latent heat buffering). Earth and Planetary Science Letters 283, 38–47.
Huber, C., Bachmann, O., Manga, M., 2010. Two competing effects of volatiles on heat transfer in crystal-rich magmas: thermal insulation vs defrosting. Journal of Petrology 51, 847–867.
Huber, C., Bachmann, O., Dufek, J., 2011. Thermo-mechanical reactivation of locked crystal mushes: melting-induced internal fracturation and assimilation processes in magmas. Earth and Planetary Science Letters 304, 443–454.
Jackson, S.E., Pearson, N.J., Griffin, W.L., Belousova, E.A., 2004. The application of laser ablation inductively coupled plasma-mass spectrometry to in situ U–Pb zircon geochronology. Chemical Geology 211 (1–2), 47–69.
Liu, Y., Hu, Z., Gao, S., Günther, D., Xu, J., Gao, C., Chen, H., 2008. In situ analysis of major and trace elements of anhydrous minerals by LA-ICP-MS without applying an internal standard. Chemical Geology 257, 34–43.
Liu, Y., Hu, Z., Zong, K., Gao, C., Gao, S., Xu, J., Chen, H., 2010. Reappraisement and refinement of zircon U–Pb isotope and trace element analyses by LA-ICP-MS. Chinese Science Bulletin 55 (15), 1535–1546.
Ludwig, K.R., 2003. Isoplot/EX version 3.0, a geochronological toolkit for Microsoft Excel. Berkeley Geochronology Center Special Publication 4, 73.
Matzel, J., Bowring, S.A., Miller, R.B., 2006. Timescales of pluton construction at differing crustal levels: examples from the Mount Stuart batholith and Tenpeak pluton, North Cascades, WA. GSA Bulletin 118 (11/12), 1412–1430.
Michel, J., Baumgartner, L., Putlitz, B., Schaltegger, U., Ovtcharova, M., 2008. Incremental growth of the Patagonian Torres del Paine laccolith over 90 k.y. Geology 36, 459–462.
Miller, J.S., Matzel, J.E.P., Miller, C.F., Burgess, S.D., Miller, R.B., 2007. Zircon growth and recycling during the assembly of large, composite arc plutons. Journal of Volcanology and Geothermal Research 167, 282–299.
Miller, C.F., Furbish, D.J., Walker, B.A., Claiborne, L.L., Koteas, G.C., Bleick, H.A., Miller, J.S., 2011. Growth of plutons by incremental emplacement of sheets in crystal-rich host: evidence from Miocene intrusions of the Colorado River region, Nevada, USA. Tectonophysics 500, 65–77.
Molina, P.G., Soto, M.F., Parada, M.A., Gutiérrez, F.J., 2013. Unraveling the La Campana gabbro cumulate emplacement and host-rock metamorphism, Coastal Range, Central Chile. Bollettino di Geofisica Teorica ed Applicata 54, 290.
Nagasawa, H., 1970. Rare earth concentrations in zircons and apatites and their host dacites and granites. Earth and Planetary Science Letters 9, 359–364.
Parada, M.A., Larrondo, P., 1999. Thermocronology of the Lower Cretaceous Caleu pluton in the Coast Range of Central Chile: tectono-stratigraphic implications. Proceedings of Fourth International Symposium of Andean Geodynamics (ISAG), Göttingen, Germany, pp. 563–566.
Parada, M.A., Larrondo, P., Guiresse, C., Roperch, P., 2002. Magmatic gradients in the Cretaceous Caleu Pluton (Central Chile): injections of pulses from a stratified magma reservoir. Gondwana Research 5, 307–324.
Parada, M.A., Féraud, G., Fuentes, F., Aguirre, L., Morata, D., Larrondo, P., 2005a. Ages and cooling history of the Early Cretaceous Caleu Pluton: testimony of a switch from a rifted to a compressional continental margin in central Chile. Journal of the Geological Society, London 162, 273–287.
Parada, M.A., Roperch, P., Guiresse, C., Ramírez, E., 2005b. Magnetic fabrics and compositional evidence for the construction of the Caleu pluton by multiple injections, Coastal Range of central Chile. Tectonophysics 399, 399–420.
Paterson, S.R., Vernon, R.H., 1995. Bursting the bubble of ballooning plutons: a return to nested diapirs emplaced by multiple processes. Geological Society of America Bulletin 107, 1356–1380.
Peytcheva, I., von Quadt, A., Georgiev, N., Ivanov, Zh., Heinrich, C.A., Frank, M., 2008. Combining trace-element compositions, U–Pb geochronology and Hf isotopes in zircons to unravel complex calcalkaline magma chambers in the Upper Cretaceous Srednogorie zone (Bulgaria). Lithos 104, 405–427.
Pupin, J.P., 1980. Zircon and granite petrology. Contributions to Mineralogy and Petrology 73, 207–220.
Rubatto, D., 2002. Zircon trace element geochemistry: partitioning with garnet and the link between U–Pb ages and metamorphism. Chemical Geology 184, 123–138.
Sano, Y., Terada, K., Fukuoka, T., 2002. High mass resolution ion microprobe analysis of rare earth elements in silicate glass, apatite and zircon: lack of matrix dependency. Chemical Geology 184, 2117–2230.
Schoene, B., Schaltegger, U., Brack, P., Latkoczy, C., Stracke, A., Günther, D., 2012. Rates of magma differentiation and emplacement in a ballooning pluton recorded by U–Pb TIMS-TEA, Adamello batholith, Italy. Earth and Planetary Science Letters 355, 162–173.
Streckeisen, A., 1976. To each plutonic rock its proper name. Earth Science Reviews 12, 1–33.
Tappa, M.J., Coleman, D.S., Mills, R.D., Samperton, K.M., 2011. The plutonic record of a silicic ignimbrite from the Latir volcanic field, New Mexico. Geochemistry, Geophysics, Geosystems 12.
Thomas, J.B., Bodnar, R.J., Shimizu, N., Sinha, A.K., 2002. Determination of zircon/melt trace element partition coefficients from SIMS analysis of melt inclusions in zircon. Geochimica et Cosmochimica Acta 66, 2887–2901.
Trail, D., Watson, E.B., Tailby, N.D., 2011. The oxidation state of Hadean magmas and implications for early Earth's atmosphere. Nature 480, 79–83.
Trail, D., Watson, E.B., Tailby, N.D., 2012. Ce and Eu anomalies in zircon as proxies for the oxidation state of magmas. Geochimica et Cosmochimica Acta 97, 70–87.
Vavra, G., 1994. Systematics of internal zircon morphology in major Variscan granitoid types. Contributions to Mineralogy and Petrology 117, 331–344.
Vergara, M., Levi, B., Nyström, J.O., Cancino, A., 1995. Jurassic and early Cretaceous island arc volcanism, extension and subsidence in the Coast Range of Central Chile. Geological Society of America Bulletin 107, 1427–1440.
Walker, G.P.L., 1986. Koolau dike complex, Oahu: intensity and origin of a sheeted-dike complex high in a Hawaiian volcanic edifice. Geology 14, 310–313.
Walker Jr., B.A., Miller, C.F., Claiborne, L. Lowery, Wooden, J.L., Miller, J.S., 2007. Geology and geochronology of the Spirit Mountain batholith, southern Nevada: implications for timescales and physical processes of batholith construction. Journal of Volcanology and Geothermal Research 167, 239–262.
Wang, X., Griffin, W.L., Chen, J., 2010. Hf contents and Zr/Hf ratios in granitic zircons. Geochemical Journal 44, 65–72.
Watson, E.B., Harrison, T.M., 1983. Zircon saturation revisited: temperature and composition effects in a variety of crustal magma types. Earth and Planetary Science Letters 64, 295–304.
Watson, E.B., Wark, D.A., Thomas, J.B., 2006. Crystallization thermometers for zircon and rutile. Contributions to Mineralogy and Petrology 151, 413–433.
Whittington, A.G., Hofmeister, A.M., Nabelek, P.I., 2009. Temperature-dependent thermal diffusivity of the Earth's crust and implications for magmatism. Nature 458, 319–321.
Wiebe, R.A., Collins, W.J., 1998. Depositional features and stratigraphic sections in granitic plutons: implications for the emplacement and crystallization of granitic magma. Journal of Structural Geology 20, 1273–1289.
Wiedenbeck, M., Allé, P., Corfu, F., Griffin, W.L., Meier, M., Oberli, F., Quadt, A.V., Roddick, J.C., Spiegel, W., 1995. Three natural zircon standards for U–Th–Pb, Lu–Hf, trace element and REE analyses. Geostandards Newsletter 19 (1), 1–23.
Wotzlaw, J., Schaltegger, U., Frick, D., Dungan, M., Gerdes, A., Günther, D., 2013. Tracking the evolution of large-volume silicic magma reservoirs from assembly to supereruption. Geology 41, 867–870.